acoustics

MDPI

Review

Laser-Induced Acoustics for Air-to-Underwater Communication: A Review of Mechanisms, Propagation, and Signal Recovery

Yang Zhao [1,2], Yingnan Chen [1], Guangyao Zhang [1], Faxiang Zhang [3] and Zhiquan Zhou [1,*]

[1] School of Information Science and Engineering, Harbin Institute of Technology (Weihai), Weihai 264209, China; zhao.yang@hit.edu.cn (Y.Z.); 25b905067@stu.hit.edu.cn (Y.C.); 24s130207@stu.hit.edu.cn (G.Z.)
[2] Weihai Key Laboratory of Intelligent Photoacoustic Detection and Sensing Technology, Weihai 264209, China
[3] Shandong Computer Science Center, Jinan 250014, China
* Correspondence: zzq@hitwh.edu.cn

Abstract

Direct air-to-underwater communication is constrained by differences between the two media, coupling at the interface, and variable sea conditions. Laser-induced acoustics offers a non-contact transmission path by converting information carried by airborne laser pulses into underwater acoustic signals at the air–water interface or within the near-surface water layer. Following the signal path from optical transmission and interface coupling to acoustic generation, underwater propagation, and signal detection, this review examines link models and the mechanisms of thermal expansion, vaporization, and optical breakdown, together with propagation constraints, particle and bubble scattering, background noise, laser-parameter effects, and communication methods. The three generation mechanisms are compared in terms of source strength, repeatability, and modulation controllability. Experimental measurements, simulations, and theoretical estimates are distinguished when interpreting representative communication results. The reviewed evidence indicates that stronger acoustic output does not necessarily yield more reliable communication: the acoustic-response duration, effective bandwidth after propagation, and receiver configuration also constrain link performance. Research now encompasses modulation and receiver processing, system prototypes, and transmission through additional interfaces. Nevertheless, link stability under variable sea conditions, reproducible error-rate performance, and field validation remain insufficiently established. Further work should prioritize quantitative modeling and system-level assessment of optoacoustic conversion efficiency and end-to-end robustness under clearly defined application requirements.

Keywords: laser-induced acoustics; optoacoustic conversion; air-to-underwater communication; modulation and coding; air–water interface coupling; remote wake-up

Academic Editors: Stéphane Moreau and Alexander Sutin

Received: 28 September 2026
Revised: 5 November 2026
Accepted: 13 November 2026
Published: 19 November 2026

Copyright: © 2026 by the author. Licensee MDPI, Basel, Switzerland. This article is an open access article distributed under the terms and conditions of the Creative Commons Attribution (CC BY) license.

1. Introduction

The development of integrated air–sea information networks has increased the demand for direct communication between aerial platforms and underwater nodes. Air and seawater differ substantially in their propagation characteristics, attenuation

mechanisms, and interface-coupling conditions. Therefore, transmission across the air–water interface often involves conversion between physical carriers, energy loss, and waveform distortion, making stable links difficult to establish [1–3]. Non-contact communication between aerial platforms and underwater nodes is particularly relevant to remote command delivery, node access, and operations in specialized environments.

Existing air-to-underwater communication systems commonly rely on cables, surface relays, or staged conversion between physical carriers. Cabled connections entail substantial deployment and maintenance costs; radio-frequency electromagnetic waves are strongly attenuated in seawater; and underwater optical communication is limited by absorption, scattering, turbidity, and alignment requirements. Although underwater acoustic communication supports long-range transmission within water, acoustic signals do not readily cross the air–water interface [4–7]. Laser-induced acoustics instead uses optoacoustic conversion at the interface or in near-surface water to convert incident laser energy into underwater sound that carries the encoded information. Thus, optical energy and encoded information can be delivered from above the water without physical contact, enabling direct air-to-underwater communication [8].

The physical basis of this approach predates contemporary communication prototypes. Lyamshev's foundational review of optoacoustic sources [9] examined sound generation through thermal expansion, surface evaporation, explosive boiling, and optical breakdown, relating these regimes to energy deposition in the liquid. Sigrist subsequently reviewed laser-generated acoustic waves in liquids and gases [10]. These works establish the source-physics foundation; they should be distinguished from later demonstrations of information transfer and from communication-oriented surveys.

Recent surveys provide complementary perspectives. Mahmud et al. [11] review cross-medium photoacoustic connectivity, technical challenges, research progress, and open problems. The Chinese-language review by Hu et al. [8] surveys optical and acoustic propagation, conversion mechanisms, signal characteristics, modulation and coding, and applications; it identifies bandwidth limitations and higher data rates as important development directions. Together, these surveys establish the broader physical and technological context for communication-oriented assessment.

The distinctive emphasis here is the relationship between generation mechanisms and end-to-end communication performance. Following the incident optical field, energy deposition, acoustic generation, underwater propagation, and receiver decisions, the review connects source strength, repeatability, and modulation controllability to the usable received bandwidth, acoustic-response duration, and symbol distinguishability. It separates conversion limitations from acoustic-channel variability and distinguishes source measurements, complete communication experiments, simulations, and theoretical estimates when comparing reported results [12–14]. This evidence-based organization complements previous surveys and relates physical mechanisms to practical link requirements. The scope is primarily the laser-induced acoustic downlink from air to underwater receivers. Reverse water-to-air communication and related non-contact sensing are discussed only as technical references, not as equivalent evidence for downlink performance.

2. Physical Principles

Laser-induced acoustic communication across the air–water interface comprises atmospheric optical transmission, interaction with the interface, acoustic-source generation, underwater propagation, and signal detection. The generation mechanism determines the pressure amplitude, spectral structure, and pulse stability; therefore, it provides the physical basis for link modeling and communication design. This section first

describes the link and then compares three representative mechanisms in terms of their suitability for communication.

2.1. Link Model

The link can be viewed as a cascade of an atmospheric optical path, optoacoustic transduction at the interface, and an underwater acoustic path [8,15]. In a typical system, information is mapped onto the on–off state, timing, repetition rate, or other controllable parameters of laser pulses. After atmospheric propagation, the laser reaches the air–water interface or near-surface water and deposits energy locally over a short period. Thermal expansion, vaporization, or optical breakdown converts this deposited energy into underwater acoustic waves. A hydrophone receives the propagated signal, and the information is recovered through synchronization, detection, and demodulation [14,16–18]. Figure 1 illustrates this process.

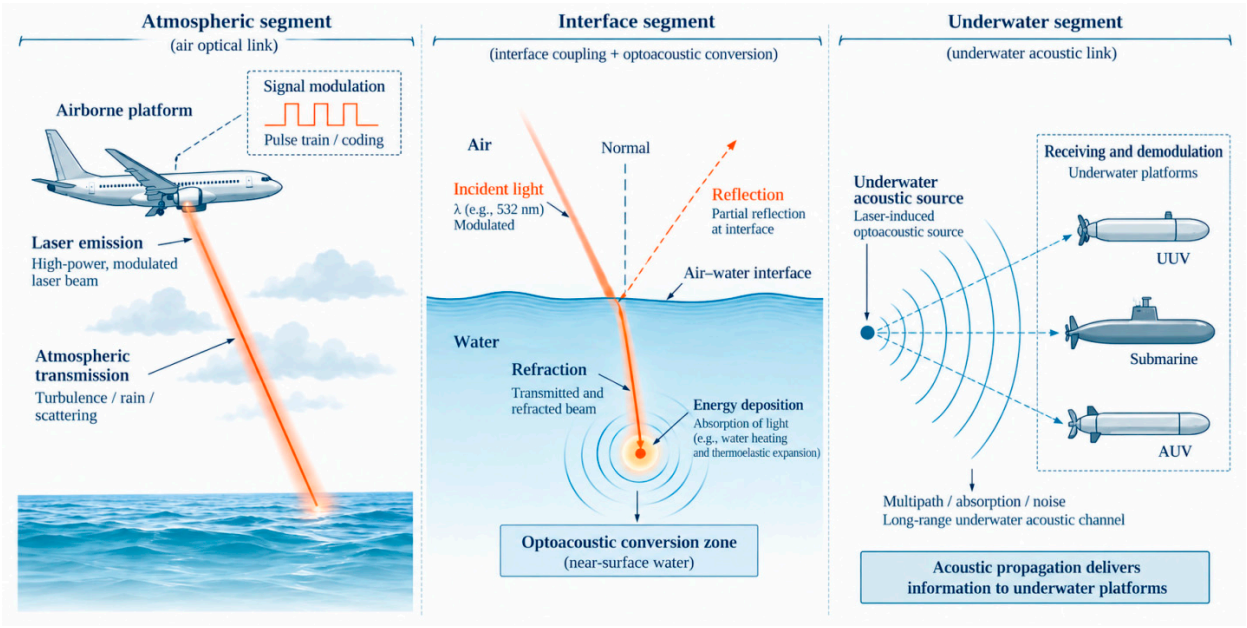


Figure 1. Link model for laser-induced acoustic air-to-underwater communication.

Communication performance is constrained at each stage: incident optical energy, energy deposition, optoacoustic conversion, underwater propagation, and receiver decisions. The optical energy reaching the interface establishes the available excitation conditions, while the location and density of energy deposition influence the dominant generation mechanism. Underwater propagation then alters the pressure and spectrum and can obscure symbol boundaries, affecting synchronization and error performance. Therefore, evaluation should consider source strength, output stability, signal preservation during propagation, and symbol distinguishability at the receiver.

2.2. Acoustic Generation Mechanisms

Laser-induced acoustics refers to the generation and outward radiation of acoustic waves following a localized, transient pressure perturbation produced by laser absorption in a liquid [9,10,19]. Depending on the energy-deposition conditions and the response of the medium, three mechanisms can be distinguished: thermal expansion, vaporization, and optical breakdown [6,9,10]. These range from a linear thermoelastic response to phase-change-assisted and plasma-dominated processes. Their principal differences concern source strength, spectral structure, repeatability, and modulation controllability.

Therefore, the mechanism influences not only how the source is formed, but also how readily the resulting signal can be modulated, transmitted, and recovered.

Early Chinese-language studies address distinct physical settings. Cui et al. [19] demonstrated laser-generated underwater sound and airborne reception of reflected acoustic signals; their tank measurements recovered a water depth of 0.74 m and detected a submerged copper plate. These results establish sensing feasibility, not digital communication performance. Su et al. [20], by contrast, modeled and measured laser-generated Rayleigh surface waves in an aluminum sample. Under their experimental conditions, line-source excitation produced stronger signals and better directivity than point-source excitation. This work is included only as a solid-state laser-ultrasonic comparison; its surface-wave results do not directly establish liquid-source behavior or underwater communication capability.

Chen and Cheng [21] combined theoretical analysis of liquid-source wavefronts with pulsed CO_2 laser experiments. They related wavefront geometry to the shape of the absorbing region and described waveform changes as excitation shifted from thermal expansion toward vaporization. In their thermoelastic measurements, the received acoustic energy was mainly below 100 kHz, with spectral peaks near 31 and 62 kHz. These observations support mechanism-sensitive waveform interpretation, but the reported spectrum belongs to that excitation and receiver configuration rather than defining a universal communication bandwidth.

2.2.1. Thermal Expansion

At low levels of energy deposition, laser absorption causes a localized, transient temperature rise. The liquid undergoes thermoelastic volume expansion and radiates pressure waves, generally without appreciable phase change or plasma formation. The source depends on the spatial and temporal distribution of heat input, the thermophysical properties of the medium, the absorption depth, and the beam-spot size. This regime offers relatively good repeatability and is amenable to modeling [22].

Studies of thermoelastic generation connect deposited heat and source geometry to the resulting pressure field [22–24]. Ye et al. [25] combined simulations with measurements using a 1064 nm laser and a 40 cm laser-spot diameter. They interpreted the two-peaked waveform as the superposition of emissions from the lower expansion surface and from the upper surface after reflection at the water–air interface. The interpeak delay was related to the absorption-defined source thickness and sound speed. The reported mean separation was approximately 0.05 ms, although the 50 kHz acquisition rate limited the precision of this timing measurement.

Zhang et al. [26] used a frequency-domain Green-function solution, inverse Fourier transformation, and numerical parameter studies to examine thermoelastic source waveforms, spectra, and directivity. In their model, shortening the laser pulse improved axial directivity while broadening the acoustic spectrum; increasing beam radius suppressed sidelobes and reduced high-frequency components at nonzero observation angles. Their propagation-distance estimates combined the calculated source with seawater spreading and absorption. These are model-dependent acoustic estimates, not measured communication ranges or bit-error rates. Applying such source models to practical links requires separate treatment of atmospheric fluctuations, surface motion, and the underwater acoustic channel.

For a homogeneous medium, a linear thermoelastic response, and small perturbations, the relationship between heat deposition and the generated acoustic pressure field can be described by an acoustic wave equation with a thermal source term:

$$\nabla^2 p(\mathbf{r},t) - \frac{1}{c^2}\frac{\partial^2 p(\mathbf{r},t)}{\partial t^2} = -\frac{\beta}{C_p}\frac{\partial H(\mathbf{r},t)}{\partial t} \tag{1}$$

where $p(\mathbf{r},t)$ is the acoustic pressure, c is the sound speed, β is the volumetric thermal expansion coefficient, C_p is the specific heat capacity at constant pressure, and $H(\mathbf{r},t)$ is the rate of heat deposition per unit volume. Equation (1) describes source generation: the temporal variation and spatial distribution of heat deposition determine the generated pressure response. Atmospheric propagation, interface fluctuations, and underwater-channel effects are not included in this equation [24].

For normal incidence, axisymmetric absorption, and the far-field approximation, the source-generated acoustic field can be expressed in the frequency domain as

$$P(r,\omega) = \frac{TI_0\beta a^2}{2C_p}\frac{\exp(ikr)}{r}\frac{\omega^2\tau_\mu}{1+\omega^2\tau_\mu^2}\exp\left(-\frac{\omega^2\tau_a^2}{4}\right)I(\omega) \tag{2}$$

with the two characteristic time scales

$$\tau_\mu = \frac{\cos\theta}{\mu c}, \qquad \tau_a = \frac{a\sin\theta}{c} \tag{3}$$

where T is the optical transmittance into the liquid, I_0 is the laser-intensity amplitude, a is the beam radius, r is the observation distance, k is the acoustic wavenumber, ω is the angular frequency, $I(\omega)$ is the frequency-domain representation of the laser pulse, μ is the optical absorption coefficient, and θ is the observation angle. The time scales τ_μ and τ_a are associated with the longitudinal absorption depth and transverse beam size, respectively. Equations (2) and (3) incorporate absorption depth and spot size into the frequency response, explaining their effects on pressure amplitude, spectral structure, and radiation directivity. Their applicability remains limited to an idealized thermoelastic source [23–25].

The well-defined parameter dependence and good pulse repeatability of thermal expansion make it a useful reference for linear link modeling, modulation and receiver analysis, and comparison with other mechanisms. Its limitations are relatively low pressure output and optoacoustic conversion efficiency. Therefore, operation over long ranges or at low signal-to-noise ratios generally requires sensitive receivers, concentrated energy deposition, or other enhancement measures.

2.2.2. Vaporization

When local energy deposition is sufficient to induce a phase change, acoustic generation shifts from a thermoelastic response to a vaporization-dominated process. Rapid evaporation creates a vapor cavity, followed by bubble expansion, oscillation, and collapse. The resulting nonlinear pressure response is governed by both the phase transition and bubble dynamics [27,28].

Multiple-pulse experiments, three-dimensional numerical analyses, and studies of pressure impulses show that vaporization can increase acoustic pressure and detectability, but may also introduce waveform tails, spectral broadening, and pulse-to-pulse fluctuations [27–30]. At higher repetition rates, the vapor cavity and local disturbance left by one pulse can modify energy deposition from subsequent pulses, reducing symbol separation and output consistency. Evidence for stronger acoustic output is relatively well established, whereas reproducible error-rate performance and long-term link stability remain less thoroughly validated. Li et al. [28] combined three-dimensional calculations of optical scattering at a rough water surface with indoor tests of vaporization-driven sound generation. They found that increasing the incidence angle

reduced the optical power density and focusing effectiveness at the surface; measured source level and optoacoustic conversion efficiency decreased markedly beyond 60° under their test conditions. This finding links interface illumination to acoustic output, but it does not establish an end-to-end communication rate or error probability.

Therefore, vaporization is relevant when the received acoustic-pressure margin is insufficient, or propagation loss is high. However, source enhancement does not necessarily improve communication quality. Pulse energy, repetition rate, and guard intervals must be coordinated to limit the influence of residual bubbles on synchronization, symbol decisions, and reliable demodulation. Residual bubbles can also modify the propagation of already generated sound through size-dependent scattering and attenuation, in addition to affecting subsequent optical energy deposition. These propagation effects are discussed separately in Section 3.3.

2.2.3. Optical Breakdown

When the local irradiance exceeds the breakdown threshold of water, strong ionization produces a hot, dense plasma. Rapid plasma expansion launches a shock wave, while subsequent bubble oscillation and collapse radiate additional acoustic energy. The resulting source has a high peak amplitude, a strongly transient response, and broad spectral content [31–33]. Thus, optical breakdown is a strongly nonlinear generation process associated with higher local energy density.

Its acoustic output depends on the breakdown threshold, plasma dimensions, shock-wave strength, and bubble dynamics. Previous work has examined plasma-formation thresholds and energy deposition in water [31,32], together with shock-wave emission, bubble generation, and subsequent evolution [33–35]. High-amplitude, broadband output is obtained at the cost of greater sensitivity to the excitation conditions and the state of the focal region.

Peak pressure alone is not sufficient to characterize a breakdown source. Zong et al. [36] combined high-speed imaging with hydrophone measurements and identified distinct emissions associated with initial expansion and subsequent bubble collapses. In their energy-sweep measurements at a fixed receiver distance, acoustic pressure increased approximately linearly with incident pulse energy. The separately resolved expansion and collapse pulses each lasted approximately 20 μs under the reported conditions. These results establish a multistage acoustic response and an experiment-specific pressure–energy relationship, rather than a measured communication rate or error probability. They do not, by themselves, quantify how the interpeak interval changes with pulse energy. Therefore, for communication, a stronger first peak must be assessed together with the later response and symbol distinguishability.

Therefore, optical breakdown may be suitable for high-loss links or applications requiring a strong source. Reliable communication nevertheless calls for closed-loop energy control, focal-region stabilization, and robust broadband reception to reduce the effects of threshold fluctuations and stochastic bubble behavior on symbol consistency and detection. The propagation effects of the associated bubble population must likewise be distinguished from its role in source generation (Section 3.3).

2.2.4. Comparison of Mechanisms for Communication

Thermal expansion, vaporization, and optical breakdown operate under different energy-deposition and medium-response conditions; no mechanism is preferable under all operating conditions. A shift from linear thermoelastic generation to phase-change or plasma-mediated processes can strengthen the acoustic output, but may also increase waveform complexity, pulse-to-pulse variability, and control requirements. Figure 2

qualitatively illustrates the trade-off between source strength and output stability. It is not a universal relationship determined by a single energy metric.

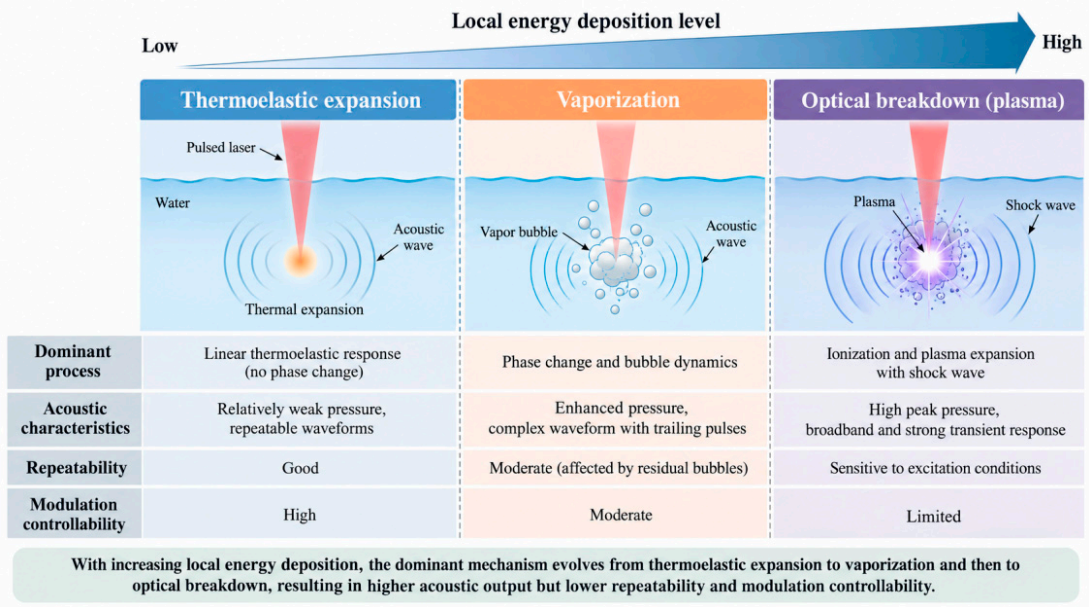


Figure 2. Acoustic generation mechanisms and their suitability for communication under different energy-deposition conditions (qualitative illustration).

As summarized in Figure 2, thermal expansion offers predictability and repeatability and serves as a reference for linear modeling and stable modulation. Vaporization can increase the detection margin in moderately lossy links, provided that residual-bubble effects and guard intervals are controlled. Optical breakdown provides a strong transient source but imposes stricter requirements on threshold control, focal stability, and receiver robustness. Therefore, mechanism selection should account for the required range, receiver sensitivity, allowable data rate, and detection complexity rather than peak pressure alone.

Therefore, acoustic generation efficiency and communication performance are different quantities. An energy-conversion efficiency compares radiated acoustic energy with optical input energy at a specified reference plane; it is not interchangeable with peak pressure measured at one range and angle. For example, Lu et al. [37] normalize the inferred acoustic energy by the laser output pulse energy and estimate the former from the pressure-squared time integral under an approximately spherical-wave assumption. This definition is not an end-to-end communication efficiency. A stronger transient or a broader source spectrum is useful only to the extent that energy remains within the propagation and receiver passbands. Longer bubble-related responses, multipath tails, and receiver ringing can require longer symbol intervals even when peak pressure increases [10,27,33,38].

Mechanism comparisons should consequently state the received effective bandwidth, waveform duration, receiver sensitivity and frequency response, propagation distance, and timing constraints alongside source output. Bit error rate (BER), data rate, and range are properties of a complete operating configuration, not intrinsic constants of thermal expansion, vaporization, or breakdown. Section 4.1.4 reports communication results only with their stated validation conditions; it does not rank mechanisms using source-pressure measurements or combine rates and error values from different operating points.

3. Propagation and Laser-Parameter Effects

The air-to-underwater link consists of atmospheric optical propagation, coupling at the air–water interface, and underwater acoustic propagation. Losses and disturbances in these stages affect energy deposition, source stability, and receiver decisions in succession. This section first considers the three propagation stages and then examines how laser parameters control the acoustic excitation conditions. Figure 3 summarizes these three propagation stages and their principal effects.

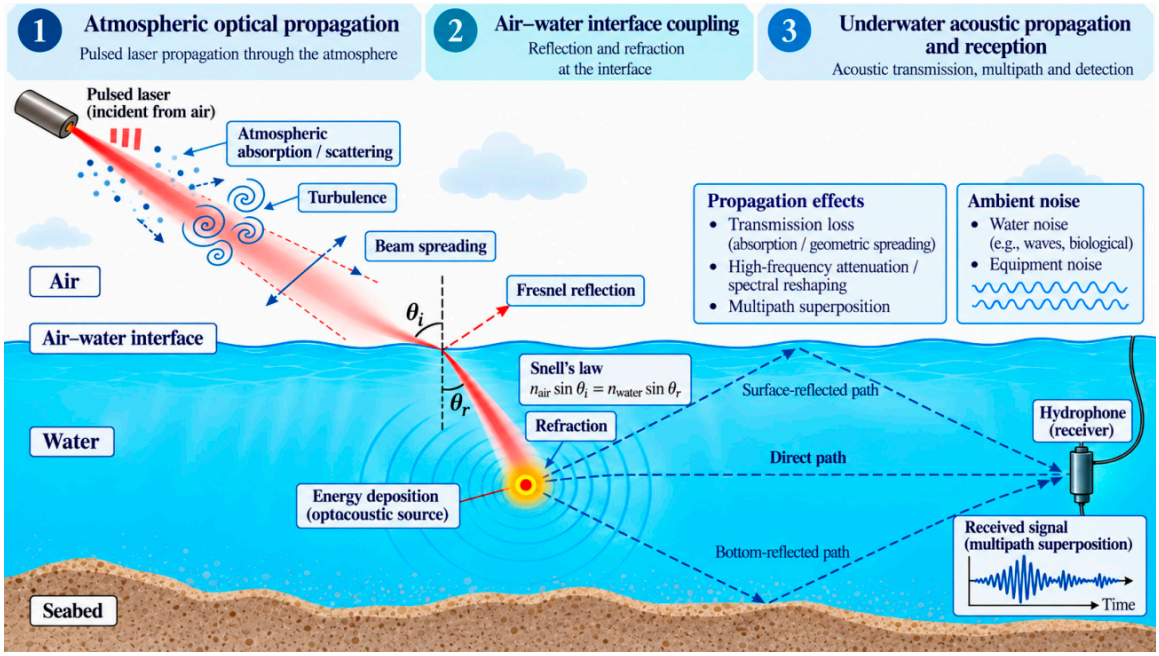


Figure 3. Propagation effects along the atmospheric, interface, and underwater sections of the link.

3.1. Atmospheric Propagation

Atmospheric effects can be separated into mean-intensity attenuation and reduced optical-field stability. Equations (4) and (5) estimate the mean intensity and transmission after propagation through the atmosphere; Equation (6) gives the Rytov variance under weak turbulence; and Equation (7) describes ideal diffraction-induced beam spreading. Together, these quantities constrain the energy available at the interface, the incident irradiance distribution, and pulse-to-pulse consistency [39–42].

The mean attenuation of a laser beam in the atmosphere is commonly described by the Beer–Lambert law:

$$I(L) = I_0 e^{-\gamma L} \tag{4}$$

where I_0 is the initial intensity, $I(L)$ is the mean intensity after propagation over a distance L, and γ is the atmospheric extinction coefficient. Equation (4) represents mean attenuation caused by absorption and scattering, not the instantaneous scintillation induced by turbulence. The optical depth depends on wavelength, path length, and the absorbing and scattering constituents along the path. For the 1.06 μm atmospheric window examined by Gan et al. [43], aerosol scattering is emphasized over molecular absorption under the stated atmospheric assumptions; the relative contributions should not be generalized to all laser wavelengths [39,40,43].

Under visibility-limited conditions, atmospheric extinction can be estimated using the empirical expression

$$\gamma(\lambda) = \frac{3.912}{V}\left(\frac{\lambda}{550\text{nm}}\right)^{-q} \tag{5}$$

where V is the visibility in kilometers, λ is the operating wavelength in nanometers, and q is an empirical parameter related to the particle-size distribution; γ is expressed in km^{-1}. Equation (5) is mainly used to estimate visibility-limited attenuation in fog, haze, and aerosol conditions. Rain-induced scattering and attenuation require a separate rain-attenuation model [41,44].

Gan et al. [43] compare visibility-based estimates for 1.06 μm transmission with reference atmospheric-transmission calculations and discuss separate rain and snow models. Their results show that the simple visibility approximation becomes less accurate in fog and that modifying the empirical exponent for low visibility improves the comparison in the examined case. The study supplies weather-dependent optical-loss estimates, not underwater attenuation measurements or an experimentally validated optoacoustic link budget. Therefore, its assumptions should be retained when estimating the optical energy available for acoustic generation.

In addition to mean attenuation, random refractive-index fluctuations cause intensity scintillation, wavefront distortion, beam wander, and beam spreading [42,45]. Under weak turbulence, the Rytov variance is commonly used to characterize turbulence-induced intensity fluctuations:

$$\sigma_R^2 = 1.23 C_n^2 k_0^{7/6} L^{11/6} \tag{6}$$

where C_n^2 is the refractive-index structure parameter, expressed in $m^{-2/3}$; $k_0 = 2\pi/\lambda$ is the optical wavenumber, and L is the propagation distance. The Rytov variance is dimensionless. This expression assumes a homogeneous path, an approximately constant refractive-index structure parameter, and plane-wave propagation under weak turbulence. To distinguish ideal diffraction from additional turbulence effects, consider a quasi-Gaussian beam with beam-quality factor M^2 in the absence of atmospheric turbulence, platform jitter, and optical aberrations. Its radius at distance L is

$$w(L) = w_0\sqrt{1 + \left(\frac{M^2 \lambda L}{\pi w_0^2}\right)^2} \tag{7}$$

where w_0 is the initial beam-waist radius, and M^2 is the beam-quality factor, with $M^2 = 1$ for an ideal fundamental Gaussian mode. Equation (7) describes deterministic spreading due to free-space diffraction; it does not represent the actual long-term spot size in turbulence. The latter requires statistical treatment of beam wander, scintillation, and turbulence-induced spreading. Optical-field fluctuations arriving at the interface cause pulse-to-pulse variations in local irradiance and acoustic output [42,45].

In summary, absorption and scattering determine the mean optical energy reaching the sea surface, weather conditions constrain optical transmission, and turbulence reduces the spatial and temporal stability of the optical field. Therefore, the atmospheric path is both an initial source of energy loss and an upstream contributor to fluctuations in acoustic generation [39,40,45].

3.2. Interface Coupling

Interface coupling connects the atmospheric optical path to underwater acoustic-source formation. Its principal effects are changes in the energy entering the water, displacement of the interaction region, and variations in generation stability. This section considers reflection and refraction, incidence and focusing, and sea-surface disturbances.

3.2.1. Reflection and Refraction

Reflection determines the fraction of incident energy entering the water, while refraction determines the direction of optical propagation in water. Reflection reduces the available optical energy; refraction shifts the high-irradiance region and the location of energy deposition. Therefore, both constrain acoustic generation near the interface [46,47].

For near-normal incidence and approximately nonabsorbing media on both sides of the interface, the Fresnel expression for power reflectance reduces to

$$R_0 = \left(\frac{n_1 - n_2}{n_1 + n_2} \right)^2 \tag{8}$$

where R_0 is the near-normal-incidence power reflectance, and n_1 and n_2 are the refractive indices of air and water, respectively. At oblique incidence, the s- and p-polarized reflectances must be calculated from the full Fresnel equations. For unpolarized light, $R = (R_s + R_p)/2$. As the incidence angle increases, the two polarization components exhibit increasingly different reflection behavior, and the total reflection loss becomes more sensitive to changes in the local surface normal. Therefore, near-normal incidence is generally favorable for maintaining stable optical-energy transmission into the water [5,46,47].

The direction of the transmitted beam is governed by Snell's law:

$$n_1 \sin \theta_i = n_2 \sin \theta_t \tag{9}$$

Refraction can change the beam direction as it crosses the air–water interface. Although it does not itself dissipate energy, it shifts the region of high irradiance. This displacement can become more pronounced at oblique incidence or under a dynamic sea surface, affecting subsequent source generation and the stability of reception [46–48].

Equation (8) gives the power reflectance near normal incidence. Under the nonabsorbing-interface approximation used here, the corresponding transmitted fraction is $1 - R_0$. Equation (9) determines the refracted direction; together with the focal-spot size in Equation (10), it helps determine the energy-deposition location and local irradiance. Reflection primarily constrains the available energy, whereas refraction and focusing govern the interaction region [48].

3.2.2. Incidence and Focusing

The incident direction and focusing conditions jointly determine the transmitted optical path, focal-region position, and local irradiance. Angular deviations shift the interaction region, while focusing controls energy concentration and the effective source dimensions. These changes affect generation efficiency, directivity, and output stability [49–51].

Incidence and focusing influence underwater acoustic output mainly by changing the focal position, interaction length, and local energy density [49,52]. Under ideal conditions, the focal-spot radius can be approximated as

$$\omega_f = \frac{\lambda f M^2}{\pi D} \tag{10}$$

where ω_f is the focal-spot radius, λ is the laser wavelength, f is the lens focal length, D is the incident beam radius, and M^2 is the beam-quality factor. Equation (10) provides a scale estimate for ideal focusing. A smaller focal spot increases local irradiance, but also makes the focal region more sensitive to sea-surface height, the local normal, and platform pointing errors [49,52].

In addition to spot size, focal position influences the source length, peak pressure, and effective range, as well as acoustic directivity and optoacoustic conversion efficiency [37,50,51]. Therefore, focusing should not be optimized solely by minimizing the spot size. Energy concentration, source dimensions, target-area coverage, the probability of maintaining the intended focal region, and pulse-to-pulse pressure fluctuations must be considered together. Zong et al. [50] found that moving the focal position changed the acoustic waveform and signal strength, whereas the acoustic-pulse width depended mainly on laser-pulse duration rather than focal position in the configurations investigated. Related work includes source characterization [51] and a qualitative theoretical analysis of radiation directivity using a plasma-disc model by Yu et al. [53]. Therefore, communication-level consequences must be assessed separately.

In distilled-water breakdown experiments, Lu et al. [37] found that conversion efficiency first increased abruptly as the focus moved below the surface. They attributed this step to the transition from a surface-interrupted bubble to a bubble able to complete its oscillation and emit collapse pulses. With further depth, the measured efficiency decreased at 1064 nm but remained approximately constant at 532 nm over the tested range; increasing the convergence angle also increased the inferred efficiency. These findings depend on the source geometry, optical path, and pressure-based energy estimate. They do not establish improved BER, data rate, or communication range.

3.2.3. Sea-Surface Disturbances

Sea-surface motion makes the air–water interface a time-varying boundary. Waves and local hydrodynamic processes change the surface height, local normal, and refracted optical path. These changes affect the focal region and energy-deposition profile, influencing source formation and link stability [54–56].

As illustrated in Figure 4, surface motion changes the optical propagation distance and effective refracted path, displacing the actual focus from its nominal position. The resulting changes in local irradiance, source length, and spatial source distribution lead to variations in acoustic directivity, amplitude, and pulse repeatability, making stable symbol reception more difficult [54–56].

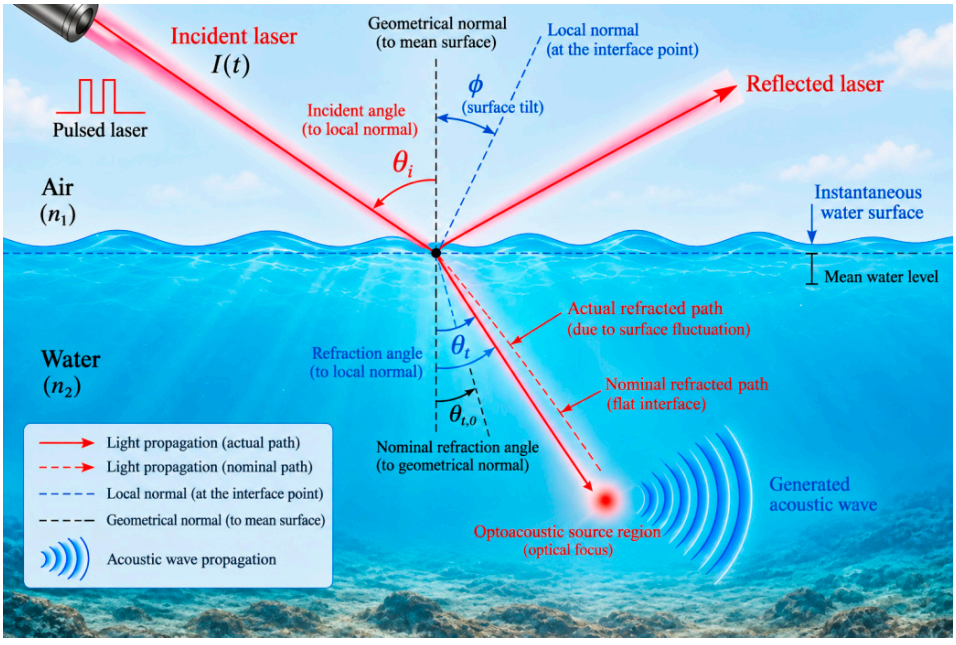


Figure 4. Effects of sea-surface disturbances on laser incidence and focal-region stability.

The resulting chain of effects links surface variation to focal displacement, acoustic-field fluctuations, and degraded reception. In addition to external interface motion, repeated excitation can produce local disturbances and residual vapor within the interaction region. To address these cumulative effects, Yang et al. proposed scanning the focal point between successive pulses, increasing signal amplitude, and reducing pulse-to-pulse fluctuations [57]. This finding supports control of the interaction region, but it does not directly validate compensation for a dynamic sea surface. The two types of disturbance should be evaluated under their respective operating conditions.

3.3. Underwater Acoustic Propagation

Once the acoustic signal is generated in water, link characterization shifts from optical-field variables to acoustic-channel parameters. Equation (11) provides a baseline for geometric spreading and absorption, while Equation (12) describes multipath superposition. Particle and bubble scattering, environmental inhomogeneity, and time variability introduce additional effects that must be assessed for the actual water body. Because laser-induced acoustic pulses are transient and often broadband, preferential high-frequency attenuation, pulse broadening, and spectral redistribution jointly affect received pressure, symbol timing, and recoverable information [38,58–62].

Relative to the sound level at a reference distance l_0, a baseline underwater transmission loss, neglecting explicit scattering losses, can be written as the sum of geometric spreading and absorption losses:

$$TL(l, f) = 10m \log_{10}\left(\frac{l}{l_0}\right) + \alpha(f)(l - l_0) \tag{11}$$

where $TL(l,f)$ is the transmission loss, in decibels, from the reference distance l_0 to distance l. The geometric spreading coefficient m is 1 for ideal cylindrical spreading and 2 for ideal spherical spreading; intermediate values may be used for shallow-water channels according to the propagation conditions. The distance unit associated with the frequency-dependent absorption coefficient $\alpha(f)$ must be consistent with those of l and l_0. Equation (11) separates geometric spreading from absorption: a broadband pulse experiences both an overall pressure reduction and preferential attenuation of high-frequency components, where $\alpha(f)$ is larger. Its effective bandwidth consequently narrows and its waveform changes [38,63]. Here, $\alpha(f)$ denotes absorption, not an unspecified total-extinction coefficient. Equation (11) does not explicitly describe scattering by particles or bubbles, multiple scattering, or boundary-induced interference; using it alone in a strongly scattering water body would omit these mechanisms.

Suspended particles redistribute acoustic energy and can attenuate the coherent signal reaching the receiver. Their acoustic size parameter is $x_a = 2\pi a_p/\lambda_a$, where a_p is a representative particle radius and $\lambda_a = c/f$ is the acoustic wavelength in water. For dilute, nonresonant small-particle scattering ($x_a \ll 1$), the Rayleigh scattering cross section has the characteristic a_p^6/λ_a^4 dependence, with a coefficient determined by material contrast. When particle dimensions approach the wavelength, the angular response and size dependence become more complex [42,64]. Therefore, concentration, size distribution, shape, and density/compressibility contrast must be considered, rather than mean size alone. Laboratory sediment measurements demonstrate the importance of mineral composition and mixed populations [64]. Optical turbidity does not by itself establish a corresponding acoustic loss: optical and acoustic wavelengths and material contrasts differ.

Bubbles require separate treatment because their compressibility can produce strong resonant acoustic scattering even when their radii are much smaller than the wavelength. For small-amplitude oscillations of an isolated, approximately spherical gas bubble at

fixed ambient pressure, the resonance frequency decreases as radius increases. Bubble concentration, radius distribution, damping, and ambient pressure determine the frequency-dependent attenuation and dispersion; a population of sizes broadens the affected frequency range [65]. Laser-produced vapor cavities are evolving, potentially nonlinear and condensing structures, so a stationary small-amplitude gas-bubble model is only a guide, not a quantitative model of every post-pulse cavity [33,65]. Therefore, for repeated excitation, bubble evolution can affect both source formation and the subsequent acoustic path. Bubble size, persistence, and population statistics are relevant to propagation as well as synchronization and demodulation.

These discrete-scatterer effects are distinct from refraction and scattering caused by spatially varying sound speed, density, and flow velocity in an inhomogeneous medium [66]. Their relative importance depends on frequency, range, and environmental conditions. A propagation assessment should identify which effects are represented explicitly rather than assign all waveform changes to optoacoustic conversion at the interface.

Theoretical and experimental studies broadly agree that frequency-selective propagation in the ocean surface layer can reduce the peak pressure of an optoacoustic pulse, increase its duration, and alter its time–frequency structure [59,61,62]. However, pulse duration, source dimensions, and receiver bandwidth differ substantially among studies, so the degree of pulse broadening cannot be compared without accounting for the experimental conditions. For communication, the bandwidth that remains usable for synchronization and detection after propagation is more informative than the initial source bandwidth alone. In liquid experiments, Li et al. [63] observed that the far-field acoustic amplitude approximately followed an inverse-distance ($1/r$) decay. This measured trend supports the geometric-spreading contribution in Equation (11), while not replacing its separate frequency-dependent absorption term. The observation characterizes acoustic propagation rather than independently demonstrating a communication data rate or error probability.

A directly measured example is provided by Zong et al. [36]: as source–hydrophone distance increased, high-frequency components decayed more rapidly, the received pulse broadened, and its spectrum shifted toward lower frequencies. Their discussion distinguishes near-source nonlinear evolution from absorption over the longer paths examined in the tank. This supports separating source generation from subsequent waveform evolution, but the reported acoustic detection distances are not measurements of successful digital communication range.

Multipath propagation introduces further distortion. A simplified frequency-domain response is

$$H(f) = \sum_{p=1}^{P} \Gamma_p \exp\left(-j2\pi f \tau_p\right) \tag{12}$$

where Γ_p is the gain of the pth path, τ_p is its arrival delay, and P is the total number of effective propagation paths. Equation (12) is a discrete multipath model that illustrates frequency-response fluctuations, waveform tails, and intersymbol interference caused by path superposition. In marine environments, currents, boundaries, and platform motion also make Γ_p and τ_p time-dependent, further complicating synchronization, equalization, and reliable demodulation [38,58,60]. Ambient noise and frequency-selective attenuation jointly determine the bandwidth from which information can ultimately be recovered [67].

Established underwater-channel studies provide context for this separation. Busacca et al. [68] compare predictive models using signal-to-noise ratio (SNR) observations from real shallow-water environments, illustrating how channel prediction and model complexity must be evaluated against measurements. Such work concerns acoustic-

channel characterization, not laser-to-sound conversion or an alternative optoacoustic transmitter. For a laser-induced acoustic link, a repeatable source can still encounter changing path gains, delays, and noise; conversely, source fluctuations should not automatically be attributed to the underwater channel. Therefore, channel estimates and source-repeatability measurements are complementary inputs to end-to-end assessment [60,68].

Figure 5 schematically summarizes two main forms of distortion during underwater acoustic propagation. Increasing range lowers the envelope peak and preferentially attenuates high-frequency components, narrowing the effective bandwidth. Reflections from the sea surface and seabed produce paths with different delays, causing pulse broadening, waveform tails, and intersymbol interference [38,58–63,67]. The schematic emphasizes spreading, frequency-selective loss, and multipath; particle and bubble scattering provide additional, environment-dependent distortions as discussed above.

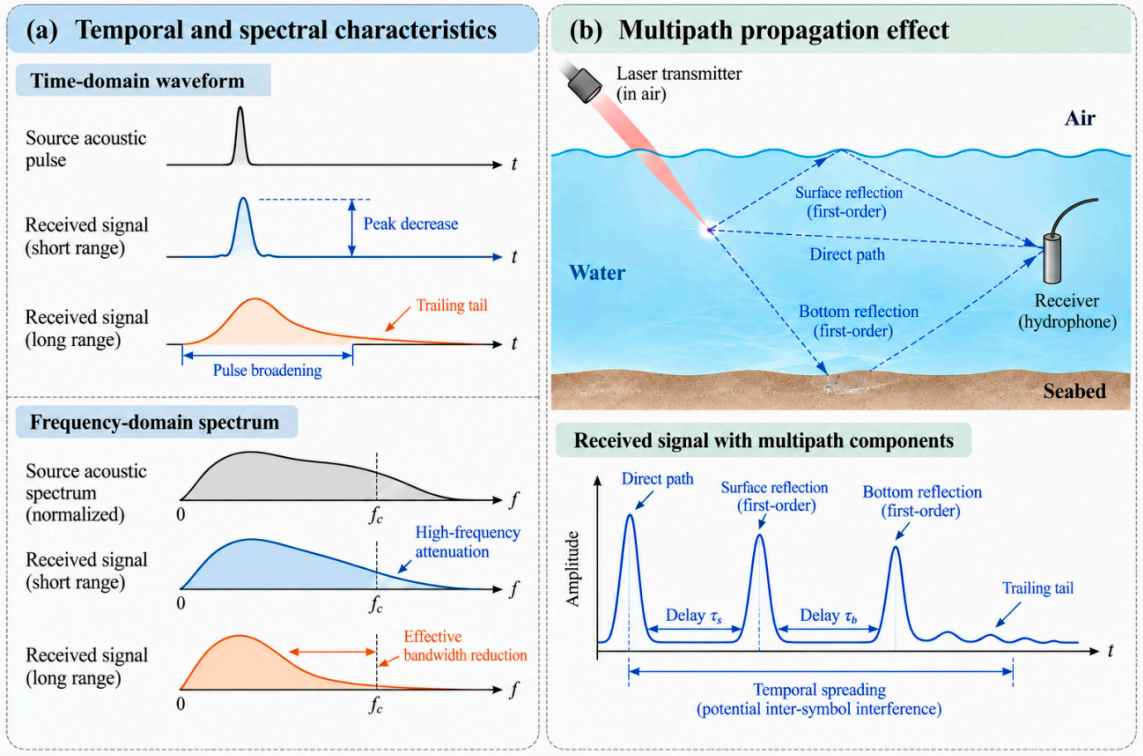


Figure 5. Schematic illustration of time–frequency changes and multipath effects during underwater acoustic propagation. The waveforms and spectra are illustrative and do not represent measured data.

Sections 3.1–3.3 show how atmospheric propagation, interface coupling, and underwater acoustic propagation impose successive constraints on the link. Table 1 summarizes the main effects and their consequences.

Table 1. Propagation constraints along a laser-induced acoustic air-to-underwater link.

Propagation Stage	Main Factors	Principal Effects on the Link
Atmospheric propagation	Absorption, scattering, turbulence, weather, and propagation distance	Reduced optical energy at the interface; beam spreading and wander; pulse-to-pulse energy fluctuations

Interface coupling	Reflection, refraction, incidence angle, focusing, and surface motion	Changes in transmitted energy, focal position, and source distribution; altered generation efficiency and stability
Underwater acoustic propagation	Geometric spreading, absorption, particle/bubble scattering, multipath, ambient noise, and channel variability	Pressure loss and spectral/temporal distortion; reduced SNR and greater synchronization, equalization, and demodulation demands

The three stages primarily affect the incident optical field, source formation, and acoustic transmission, respectively. Their accumulated losses and disturbances constrain the received signal-to-noise ratio (SNR), synchronization reliability, and demodulation performance.

3.4. Effects of Laser Parameters on Source Characteristics

In addition to environmental conditions, wavelength, pulse energy, pulse duration, spot size, and repetition rate primarily influence the absorption depth, deposited energy, energy-release time scale, interaction dimensions, and pulse-sequence timing, respectively. Building on the mechanisms discussed in Section 2.2, this section relates these adjustable parameters to acoustic pressure, spectral content, and pulse-sequence characteristics.

3.4.1. Wavelength

Laser wavelength affects atmospheric transmittance, optical absorption and scattering in water, and the location and spatial distribution of energy deposition. Its selection should balance transmission across the media with local generation conditions rather than minimize loss in only one part of the link.

Optical attenuation in seawater contains distinct absorption and scattering contributions. The blue–green region generally has lower attenuation in many water types, but this is not universal [69,70]. Here, "scattering conditions" refers specifically to the concentrations, size distributions, shapes, and optical properties of suspended particles and bubbles, including their refractive-index contrast with water. Absorption deposits energy locally, whereas scattering redirects light and can reduce the ballistic energy delivered to the intended focal region. Scattered light is not necessarily lost from the water; its subsequent absorption can redistribute heating and change the acoustic-source geometry [42,69,70].

The relevant optical size parameter is $x_o = 2\pi a_p/\lambda_w$, where λ_w is the wavelength in water (the vacuum wavelength divided by the refractive index). In the small, weakly absorbing, approximately spherical particle limit, the Rayleigh scattering cross section varies approximately as a_p^6/λ_w^4 at fixed refractive-index contrast. When particle size is comparable to or larger than the wavelength, Mie-type or geometric scattering becomes important, often with a pronounced forward component; the wavelength dependence is no longer a universal inverse-fourth-power law [42,71]. Actual attenuation requires integration over the particle-size distribution and inclusion of absorption. These optical effects govern energy delivery before sound generation and must not be conflated with the acoustic size parameter in Section 3.3.

Wavelength also affects energy deposition and the resulting acoustic output. Nanosecond excitation at 1064 and 2940 nm produces appreciably different shock responses in water [72], while changes in absorption conditions alter acoustic-signal strength and peak frequency [73]. Wavelength selection should consequently be specific

to the target water body and required range, matching absorption depth and source stability to reception requirements [13]. Low optical propagation loss alone does not guarantee efficient sound generation: weak absorption distributes deposition over a larger volume, while strong absorption confines heating closer to the interface. Therefore, water-specific absorption and scattering should be assessed together with source localization and repeatability.

3.4.2. Pulse Energy

Pulse energy affects pressure output through local energy deposition, and its influence must be interpreted alongside incidence, focusing, and the dominant generation mechanism. In the breakdown experiments of Zong et al. [36], pressure increased approximately linearly with energy over the tested range at a fixed receiver distance. This is a configuration-specific observation rather than a universal scaling law across generation regimes. Changes in the complete acoustic waveform must be evaluated separately from changes in its peak amplitude [36,74].

Mechanism transitions and the associated nonlinear responses were discussed in Section 2.2 [31,33,75]. From a parameter-design perspective, the improvement in received signal strength from higher pulse energy remains constrained by focusing conditions and propagation loss. Therefore, pressure enhancement should be evaluated together with waveform consistency and error performance.

3.4.3. Pulse Duration

Pulse duration here refers to the duration of an individual laser pulse. It determines the time scale of energy release and the peak power, thereby affecting the spatial structure of the source and the time–frequency characteristics of the acoustic signal.

Intense femtosecond pulses can generate pronounced nonlinear effects and acoustic emission during propagation in water [76]. Filamentation of terawatt ultrashort pulses can also create axially extended sources on the centimeter scale [77]. Therefore, shortening the pulse may change the deposition geometry from localized to extended, in addition to increasing the instantaneous power.

Brelet et al. characterized a broadband underwater acoustic source with a reported spectrum spanning at least the 0.1–10 MHz range under the conditions investigated [75]. This result is specific to the source and measurement configuration and should not be interpreted as a universal bandwidth for ultrashort-pulse excitation. Yellaiah and Prem Kiran compared acoustic signals generated with 10 ns and 30 ps laser pulses under similar experimental conditions, illustrating why pulse-duration effects must be evaluated together with pulse energy and propagation [61]. For communication design, the relevant quantities are the received waveform, usable acoustic bandwidth, and receiver time resolution rather than pulse duration alone.

3.4.4. Spot Size

Spot size controls both the transverse energy density and the effective acoustic-source dimensions. At fixed pulse energy and duration, a smaller spot increases local irradiance and more readily triggers vaporization or breakdown. A larger spot distributes energy more broadly and can offer greater tolerance to focal displacement and interface disturbances.

Experiments and numerical studies show that the incident optical-field distribution strongly influences acoustic amplitude and waveform shape [78,79]. At fixed total energy, higher local irradiance from a smaller spot does not guarantee higher pressure in every observation direction. For example, Zhang et al. [26] found that increasing beam radius left the on-axis pressure and spectrum unchanged in their fixed-energy thermoelastic

model, while suppressing sidelobes and narrowing the spectrum off-axis. This directional dependence should be distinguished from the increased likelihood of mechanism transitions when energy is concentrated into a smaller spot.

A larger illuminated region can produce a more extended source and a slower pressure buildup. High-frequency components may be suppressed, shifting the spectral centroid toward lower frequencies [62]. Therefore, spot-size selection must balance local energy density, source dimensions, directivity, coverage, and tolerance to interface disturbances [23,25].

3.4.5. Repetition Rate

With single-pulse energy and incidence conditions held constant, the repetition rate mainly determines the interval between acoustic responses, the spectral structure of the pulse train, and the ability to sustain transmission. It does not directly change the energy deposited by an individual pulse.

Berthelot analyzed narrow-band thermoacoustic generation in water using high-repetition-rate laser pulses and showed that effective spectral concentration depends on matching the repetition rate to the excitation conditions [80]. The predicted optimum is specific to the model and optical configuration, rather than a universal operating range for communication. In a related but distinct application, Kaleris et al. demonstrated pulse-amplitude-modulated sound reproduction in air using laser excitation of a metal target [81]. That study provides a reference for pulse-train modulation and waveform fidelity, but it does not validate an optimum repetition rate for underwater communication.

Repetition rate can also serve directly as an information-bearing parameter and support more continuous sound generation and more efficient transmission [82,83]. However, it should not be equated with achievable data rate. Recovery of the source and acoustic response, guard intervals, spectral concentration, and receiver detection capability must be considered together.

3.4.6. Comparison of Parameter Effects

Figure 6 qualitatively summarizes representative effects of pulse energy, pulse duration, spot size, and repetition rate on acoustic output. The curves are conceptual illustrations rather than fits to measurements obtained under a common experimental configuration; they should not be interpreted as universal quantitative relationships. In particular, the usable repetition-rate range depends on the acoustic response, transmission timing, and receiver conditions; transmission efficiency and source stability are distinct evaluation criteria.

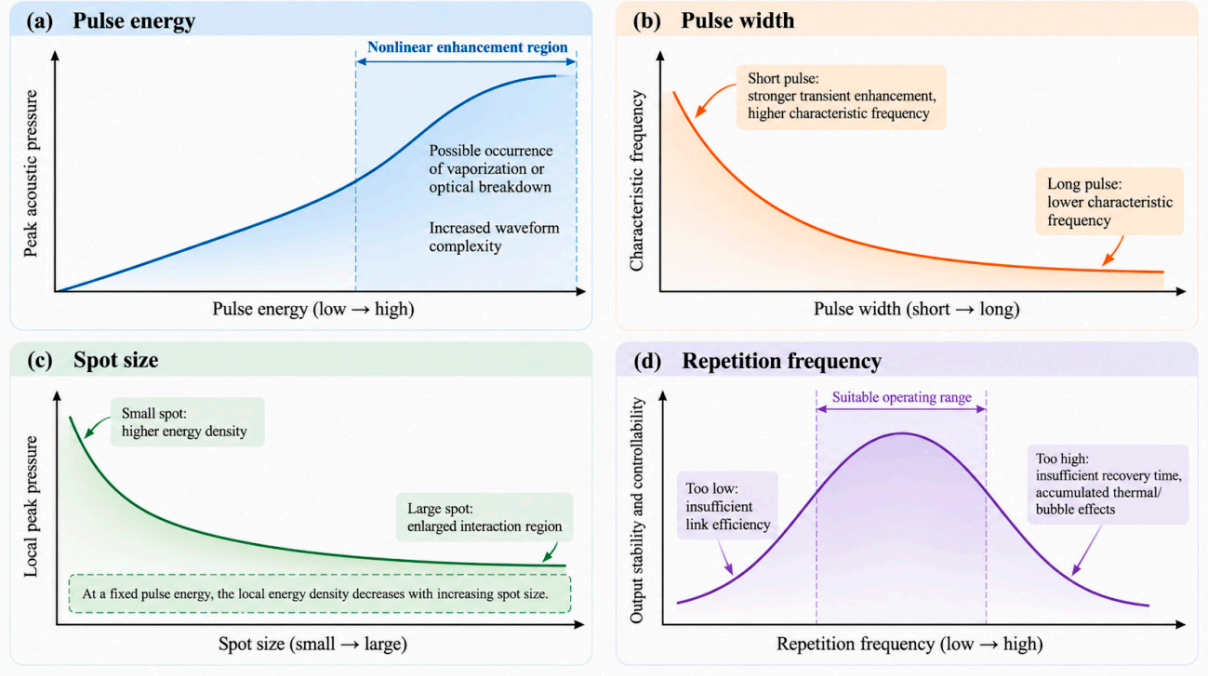


Figure 6. Representative effects of pulse energy, pulse duration, spot size, and repetition rate on acoustic output (qualitative illustration).

Complementing the qualitative trends in Figure 6, Table 2 summarizes how wavelength and the other parameters affect energy deposition, source formation, and communication performance.

Table 2. Effects of the main laser parameters on laser-induced acoustic communication.

Parameter	Primary Role	Typical Effects	Design Considerations
Wavelength	Governs atmospheric transmission, optical absorption and scattering in water, and energy-deposition depth	Changes focal energy delivery, source location, generation conditions, and stability	Balance water-specific absorption/scattering, particle size relative to optical wavelength, and conversion efficiency
Pulse energy	Controls local energy deposition per excitation	Changes pressure amplitude and may trigger mechanism transitions	Consider stability alongside stronger output
Pulse duration	Controls the deposition time scale and peak power	Changes source dimensions, transient response, and spectrum	Match transient enhancement and bandwidth to propagation
Spot size	Controls transverse energy density and effective source size	Changes pressure, spectral centroid, and radiation pattern	Balance energy concentration and source dimensions
Repetition rate	Controls pulse timing and response superposition	Changes spectral structure, sustained output, and information encoding	Balance spectral concentration, throughput, and detection

Wavelength, pulse energy, pulse duration, and spot size primarily govern single-pulse deposition and source characteristics, whereas repetition rate has a stronger influence on pulse-sequence organization and sustained transmission. Therefore, parameter selection should move beyond optimizing a single metric and instead balance range, usable bandwidth, data rate, output stability, and pointing-control requirements.

4. Communication Techniques

Given the generation mechanisms and propagation constraints, communication design seeks to map information onto controllable laser parameters and recover it reliably from a distorted acoustic field. Existing work addresses modulation and coding, receiver processing, and experimental systems. Modulation determines symbol mapping and potential data rate, receiver processing affects synchronization and detection reliability, and experimental systems establish link feasibility. This section compares these approaches in terms of data rate, error performance, robustness, and implementation complexity.

4.1. Modulation and Coding

Modulation and coding map a bit sequence onto controllable laser-pulse parameters while allowing the receiver to distinguish symbols despite acoustic tails, interpulse interference, and nonlinear recovery constraints. For comparison, Figure 7 groups the approaches into three broad categories. Time-domain pulse modulation uses pulse presence, pulse-train duration, position, or spacing; frequency-based and multilevel modulation expand the symbol set through frequency states, frequency combinations, or focusing states; and coding supports synchronization, error control, and pulse-sequence constraints. These approaches offer different trade-offs among data rate, detection robustness, and implementation complexity.

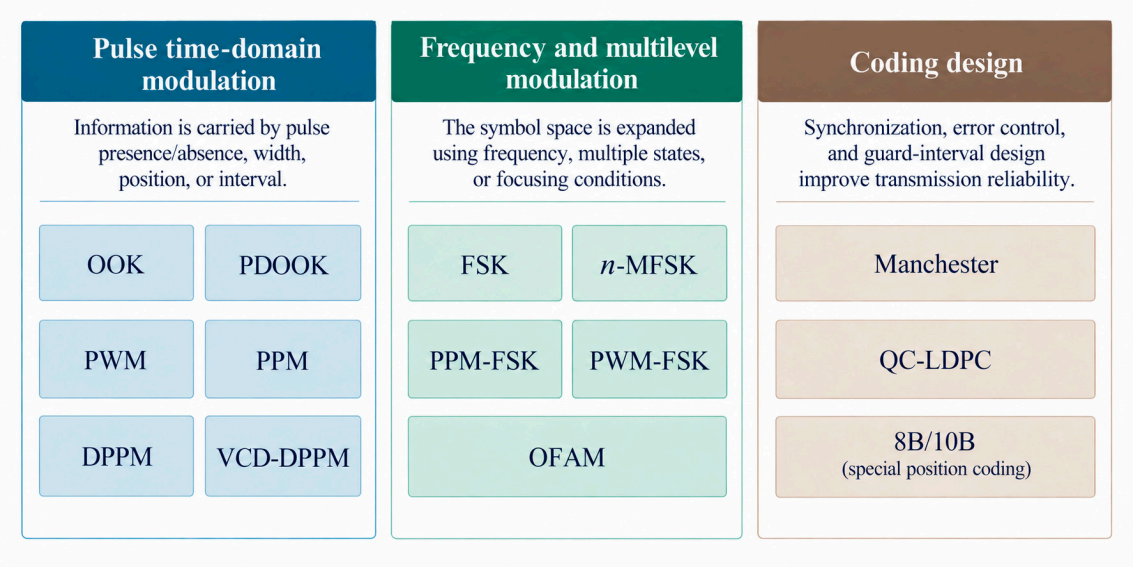


Figure 7. Modulation, detection, and coding approaches for laser-induced acoustic air-to-underwater communication. Acronyms are spelled out in the following text. Peak-detection-based on–off keying (PDOOK) modifies the receiver decision strategy of on–off keying (OOK) [84]; it does not introduce an independent information-mapping dimension. The diagram includes modulation schemes, detection refinements, and coding approaches, so its branches are not mutually exclusive.

Figure 8 illustrates the symbol mappings used by representative schemes. On–off keying (OOK), pulse-width modulation (PWM), and pulse-position modulation (PPM) encode information through pulse presence, pulse-train envelope duration, and time-slot position, respectively. Frequency-shift keying (FSK) creates frequency states by switching the repetition rate; *n*-multiple-frequency-shift keying (*n*-MFSK) expands the symbol set through multiple-frequency combinations; and optical focusing-based adaptive modulation (OFAM) uses focusing changes to produce distinguishable pressure levels.

The diagram illustrates mapping dimensions and symbol structures, not a common set of laser parameters, symbol durations, or experimental conditions [84–95]. The PWM width shown is the temporal envelope of a communication pulse train and should not be confused with the individual laser-pulse duration discussed in Section 3.4.3. Throughout this review, PPM denotes pulse-position modulation, not parts per million.

4.1.1. Time-Domain Pulse Modulation

Time-domain pulse modulation encodes information through pulse presence, pulse-train duration, slot position, or interpulse spacing and has been widely studied in this field. Performance depends not only on the symbol interval, but also on whether adjacent symbols remain distinguishable in the presence of acoustic tails, overlapping responses, and noise [84–86].

OOK represents binary information by emitting or withholding a laser pulse. It is simple to implement, but its information content per symbol is limited by binary mapping. The peak-detection-based OOK scheme (PDOOK) proposed by Islam et al. retains this mapping while refining the receiver's first-peak decision strategy [84]. Detection and synchronization are discussed in Section 4.2.1.

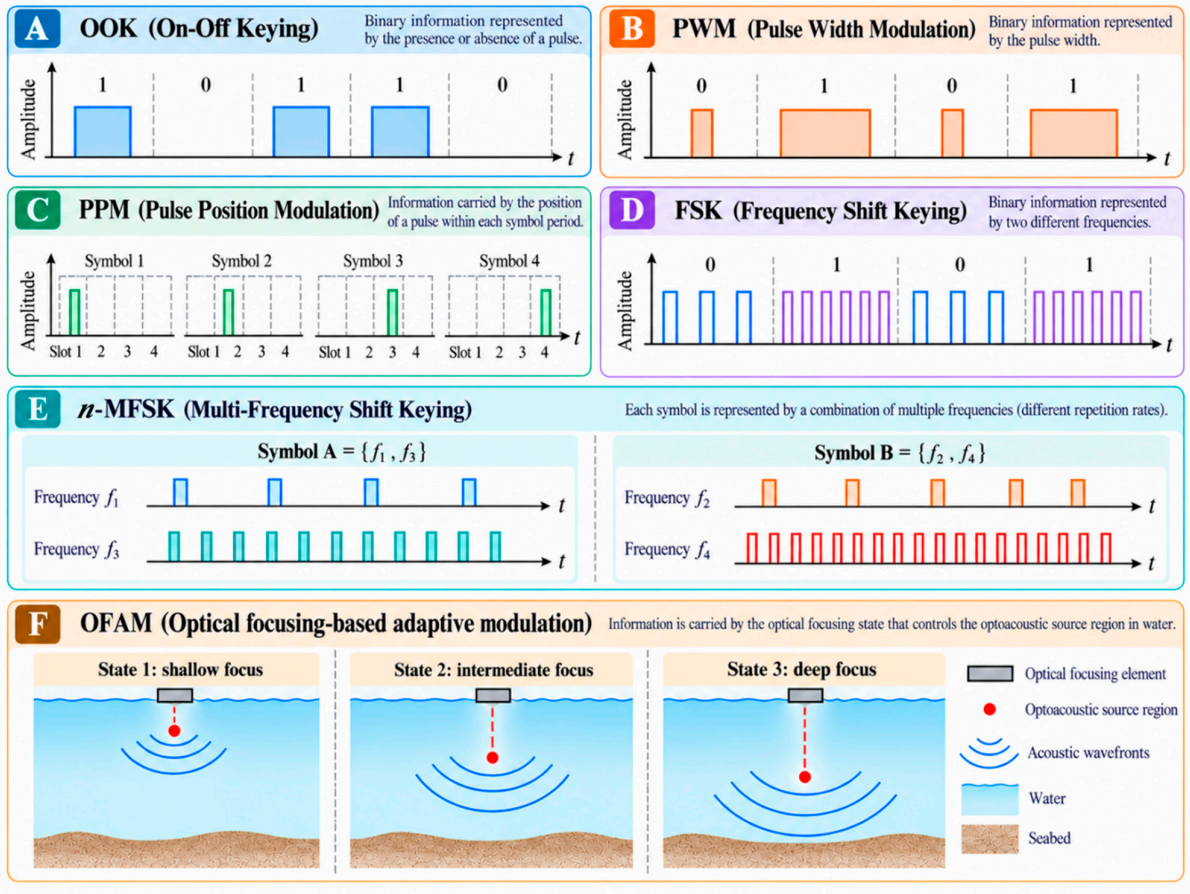


Figure 8. Symbol mappings for representative laser-induced acoustic modulation schemes. In (**A**), (**B**), and (**D**), 0 and 1 denote binary data. In (**C**), Symbols 1–4 label successive symbol intervals, each divided into Slots 1–4. In (**E**), Symbols A and B are encoded by the indicated combinations of pulse repetition frequencies f_1–f_4. In (F), States 1–3 denote shallow, intermediate, and deep focusing, respectively.

In the PWM scheme of Chen et al. [87], each two-bit group is mapped to a six-slot pulse train, including two leading occupied slots. Varying the number of emitted pulses changes the acoustic-envelope duration, not the 10 ns duration of each optical pulse. Reception uses a distributed-feedback fiber-laser (DFB-FL) hydrophone, filtering, sliding-window localization, and energy-based decisions within each symbol. At a laser repetition rate of 400 Hz, the six-slot symbol lasts 6/400 s; the paper reports approximately 130 bit/s and 8% BER at this operating condition. At 500 Hz, BER exceeds 15% in the same study. The result demonstrates laboratory information transfer with a specific receiver and processing chain, not a general optimum repetition rate or validated sea-state robustness.

PPM encodes information in time-slot positions and aims to increase the information carried by each pulse. An efficient PPM scheme achieved approximately 3.2 times the OOK bit rate for t_p = 1.0 ms and M = 4 [85]. Liao et al. [86] implemented byte-framed time-slot hopping among 256-, 16-, and 4-PPM, with FPGA encoding and decoding. Their still-water-tank test used 10 ms slots and demonstrated character transmission at 8 bit/s over an approximately 1.3 m acoustic source–receiver path. The experimental laser had a maximum repetition rate of 50 Hz. These measured conditions differ from the proposed 10 μs-slot configuration associated with a theoretical rate of approximately 5 kbit/s.

The same paper separately reports an error rate below 10^{-5} in repeated transmissions at a higher water-surface pulse energy, approximately 25 mJ [86]. Its English abstract identifies this metric as SER, whereas the Chinese text uses a less specific error-rate description. The comparison in Section 4.1.4 preserves that distinction and lists the error test separately from both the 8 bit/s transmission example and the 5 kbit/s projection. The latter assumes sufficient laser repetition rate and response capability and is not measured end-to-end throughput. Accurate slot synchronization, guard intervals, and explicit error-counting procedures remain essential to interpreting such results.

Under nonlinear excitation, time-domain modulation must also account for suppression of subsequent optoacoustic conversion by a vapor cloud. Mahmud et al. introduced vapor-cloud-delayed differential pulse-position modulation (VCD-DPPM), incorporating a vapor-cloud delay into the interpulse-spacing constraints [88]. Under the nonlinear conditions studied, a recovery time of approximately 1 ms was required between pulses when the laser repetition rate exceeded 1000 Hz. In text-transmission simulations at 10 kHz and 40 Hz, the VCD-DPPM symbol rate was approximately 6.9 and 1.69 times that of OOK, respectively, with a reported power-efficiency improvement of approximately 137% [88]. The significance of this approach is that it incorporates nonlinear source recovery into symbol timing rather than relying on repetition-rate increases alone.

A common constraint on time-domain schemes is the trade-off between acoustic-response duration and symbol spacing. OOK and PWM are straightforward, while PPM and differential PPM increase the information carried per pulse. Their theoretical gains can translate into reliable throughput only when recovery time, guard intervals, and synchronization errors are adequately controlled.

4.1.2. Frequency and Multilevel Modulation

In addition to temporal parameters, symbols can be constructed from the acoustic fundamental frequency, laser repetition rate, combinations of frequencies, or focusing states. These approaches increase the number of distinguishable states, but remain constrained by source strength, frequency resolution, propagation attenuation, and receiver classification capability [89–91].

Not every repetition-rate-controlled scheme is conventional FSK. He et al. [89] demonstrated tunable-fundamental-frequency amplitude-shift keying (ASK), using an 11-position frame comprising two pilot positions, eight data positions, and one end

marker. The pilot interval identifies the pulse-repetition setting used within each frame. Their laboratory example used 10, 15, and 20 Hz settings within a 1–20 Hz laser repetition-rate range and showed recovery of the transmitted digital waveform after hydrophone reception, filtering, and shaping. These values describe the pulse/slot timing used within each frame, not acoustic carrier frequencies of 10–20 Hz. The paper does not provide a quantified BER, net data rate, or communication-range result; it supports frame-based signal recovery rather than a numerical FSK performance comparison.

Repetition-rate control has also been studied for speech transmission [83]. For frequency-state mapping, Chen et al. combined a pulsed laser with a DFB-FL acoustic sensor and demonstrated FSK with up to 16 frequency states at a 250 Hz laser repetition rate, achieving a maximum rate of 53 bit/s [92]. Frequency-state detection can reduce sensitivity to amplitude fluctuations, but higher-order FSK remains limited by the number and spacing of usable frequencies, observation duration, and received SNR.

Multiple-frequency modulation expands the symbol set through frequency combinations. Huang et al. [91] analyze thermal-expansion-based n-MFSK using long-pulse and high-repetition-rate implementations and numerical validation. For $n = 2$, their modeled 2-MFSK rate is twice that of conventional 2-FSK. However, increasing the number of frequency components distributes the available energy among them and places greater demands on frequency resolution and joint detection. When the received pressure margin is limited, a higher data rate may come at the expense of range. Therefore, the benefit should be evaluated under comparable energy constraints and error-rate criteria, rather than inferred solely from the number of symbol states.

Frequency can also be combined with pulse position or duration in hybrid schemes. The Chinese patents in [93,94] propose PPM-FSK and PWM-FSK arrangements: the former maps symbols jointly onto position and frequency, whereas the latter combines pulse-train duration and frequency. These are proposed modulation/device configurations, not by themselves evidence of field-validated throughput. Relative to a single-parameter scheme, these methods distribute symbol discrimination across multiple dimensions and enlarge the symbol set. The trade-off is more complex transmitter control, synchronization, and joint parameter detection. For the reverse water-to-air link, Zhou et al. [90] simulated the relationship between underwater acoustic excitation and surface displacement, followed by optical-interferometric demodulation. Their comparison showed a modulation-dependent trade-off: binary ASK required a lower SNR at a target BER of 0.001 than the tested FSK and phase-shift-keying (PSK) schemes, whereas binary PSK supported the highest simulated maximum data rate among the compared formats. These results illustrate receiver and modulation trade-offs within the modeled uplink, not the measured performance of the laser-induced acoustic downlink.

OFAM is a representative multilevel approach. Mahmud et al. mapped focusing states to sound-pressure levels and addressed data-rate and power-efficiency constraints associated with vapor-cloud accumulation [95]. The study reported data rates approximately 6 and 4.4 times the respective PDOOK baselines for fixed-focus OFAM-1D and dynamic-focus OFAM-3D. It also reported power-efficiency improvements of approximately 137% for both variants and used machine learning to assist multistate demodulation. The work combined pressure measurements with communication modeling or simulation. These relative gains must be interpreted using each variant's baseline configuration and timing constraints, and do not establish a ranking of the variants by absolute data rate. Therefore, the comparison in Section 4.1.4 reports only the relative data rates and does not combine them with error results from other conditions as a single measured performance point.

4.1.3. Coding

Coding primarily supports clock synchronization, error control, and pulse-sequence constraints. It acts on the transmitted bit sequence rather than directly on the acoustic generation mechanism, using bit-pattern constraints, redundancy, or sequence restrictions to improve reception reliability [96–98].

Manchester coding uses a prescribed transition within each bit interval to assist clock recovery and is suitable for relatively simple synchronization. The patent in [96] proposes combining Manchester coding with pulsed laser transmission to reduce timing drift during long runs of identical bits. However, the coding overhead must be considered when assessing the achievable information rate.

Quasi-cyclic low-density parity-check (QC-LDPC) coding addresses error control. The patent in [97] proposes its use in the air-to-underwater downlink to improve information recovery through coding gain. The patent addresses the downlink and should not be interpreted as validation of bidirectional communication. Redundancy, decoding effort, and frame-design requirements increase, making the approach more relevant when reliability takes priority, and sufficient receiver processing capacity is available.

The 8B/10B special-position coding method illustrates how coding can constrain physical interpulse spacing. To address closely spaced pulses in PPM driven by a low-repetition-rate laser, Hu et al. used 8B/10B coding to limit long runs of identical bits, together with odd–even alternation, position mapping, and empty code positions to create guard regions [98]. The approach reduces the impact of back-to-back pulses on detection and illustrates the role of coding in organizing pulse sequences and guard intervals, in addition to conventional error-control functions.

These studies indicate that coding should account for the physical timing constraints of optoacoustic pulses. Manchester coding emphasizes clock recovery, QC-LDPC provides error correction, and 8B/10B special-position coding helps organize pulse spacing and guard regions. Future designs should balance redundancy, acoustic recovery time, and receiver computation rather than apply conventional codes without adaptation.

4.1.4. Comparison of Methods

Data rate, bit error rate (BER), and symbol error rate (SER) are important measures of modulation performance. However, reported studies differ substantially in laser parameters, range, receiver bandwidth, generation mechanism, and type of validation. Table 3 organizes representative results by evidence type and lists experimental transmission results separately from theoretical rate estimates, including when both concern the same method. The values describe performance under the original study conditions and are not intended as an absolute ranking across publications.

Table 3. Communication performance of representative modulation schemes. Created by the authors based on the cited literature.

Method	Evidence and Conditions	Reported Rate/Relative Gain	BER/SER	Features and Constraints	Ref.
OOK	Experiment summarized in [87]; 100 Hz laser repetition rate	60 bit/s	BER: 4.2%	Simple implementation; binary mapping	[12,87]
PDOOK	Experiment + simulation; peak detection	Approx. 20 bit/s	Simulated BER curves; no single measured value compiled	First-peak detection; binary mapping	[84]

PWM	Laboratory experiment; 400 Hz; DFB-FL receiver; 2 bits/6 slots	Approx. 130 bit/s	BER: 8%	Pulse-train duration and energy decisions; cooler-noise filtering	[87]
Efficient PPM	Experiment + simulation; t_p = 1 ms, M = 4	Approx. 3.2× OOK	—	More information per pulse; timing sensitive	[85]
Time-slot-hopping PPM (transmission test)	Tank experiment; 10 ms slots; approx. 1.3 m acoustic path	8 bit/s	—	Byte-framed FPGA transmission; see separate error test below	[86]
Time-slot-hopping PPM (error test)	Repeated transmissions; water-surface energy near 25 mJ (see note)	—	Reported <10^{-5} (SER in English abstract)	Counting procedure unspecified; not a 5 kbit/s result	[86]
Time-slot-hopping PPM (theory)	10 μs slots; assumed repetition rate and system response	Theoretical: approx. 5 kbit/s	Not applicable: rate estimate only	Not measured end-to-end throughput	[86]
VCD-DPPM	Simulation; 40 Hz/10 kHz	Symbol rate: approx. 1.69×/6.9× OOK	—	Accounts for vapor-cloud recovery; complex timing	[88]
16-FSK	Experiment; 250 Hz laser repetition rate; convolution-based demodulation	Up to 53 bit/s	BER curves at different SNRs	High-order frequency-resolution requirements	[92]
n-MFSK	Theory + simulation; n = 2	2-MFSK: 2× 2-FSK	—	Frequency-domain expansion; lower pressure per frequency	[91]
OFAM-1D	Pressure measurements + communication modeling/simulation; fixed focus	Approx. 6× its PDOOK baseline	—	Multilevel mapping; requires stable focusing	[95]
OFAM-3D	Pressure measurements + communication modeling/simulation; dynamic focus	Approx. 4.4× its PDOOK baseline	—	Complex control; study-specific baseline	[95]

Note: Theoretical and simulated rates are not measured end-to-end throughput; BER and SER are not interchangeable. The OOK benchmark is summarized in [87] and attributed there to [12]. For time-slot-hopping PPM [86], the 8 bit/s example uses 10 ms slots. A separate repeated-transmission statement reports an error rate below 10^{-5} at 25 mJ incident on the water surface; the English abstract calls it SER and states an energy greater than 25 mJ. The total tested bits/symbols and the error-counting procedure are not specified, so this result is retained as a qualified report, not converted to BER or paired with the 5 kbit/s projection. For OFAM, only relative data rates are listed; the two PDOOK baselines and timing constraints need not be identical. The absence of entries in Table 3 means that single appropriate values are not offered here, rather than that no values were offered in the referenced studies. Maximum rates and minimum error values should not be assumed to describe the same operating point.

The explicitly reported experimental rates in Table 3 span single-digit to low-hundreds of bits per second; this selection does not define the performance limit of the field. Potential gains from theory and modeling remain conditional on timing, focusing control, and receiver performance. Comparisons require excitation conditions, propagation distance, receiver bandwidth, and error definitions to be reported together. For example, the OOK benchmark of 60 bit/s with BER 4.2%, attributed to Zhao et al. [12] in the comparison by Chen et al. [87], and the latter's PWM result of approximately 130 bit/s with BER 8% use different laser repetition rates and signal processing. Their numerical values do not isolate a generation-mechanism advantage. Range should distinguish the atmospheric optical path from the underwater acoustic path; detecting a pulse at a stated distance is not equivalent to recovering information at that distance.

4.2. Receiver Processing

Receiver processing extracts useful symbol features from distorted acoustic signals and recovers the transmitted information. Oscillatory tails, amplitude fluctuations, multipath, and ambient noise require coordinated preprocessing, feature extraction, timing synchronization, and channel compensation.

Figure 9 summarizes acoustic reception, analog front-end conditioning and sampling, filtering and denoising, optional channel equalization, feature extraction, timing recovery and synchronization, symbol decisions, and decoding. Synchronization refers to pulse and symbol timing rather than spatial localization. The diagram is a functional schematic; the ordering and joint implementation of these functions depend on the receiver architecture. Channel equalization is discussed further in Section 4.2.2.

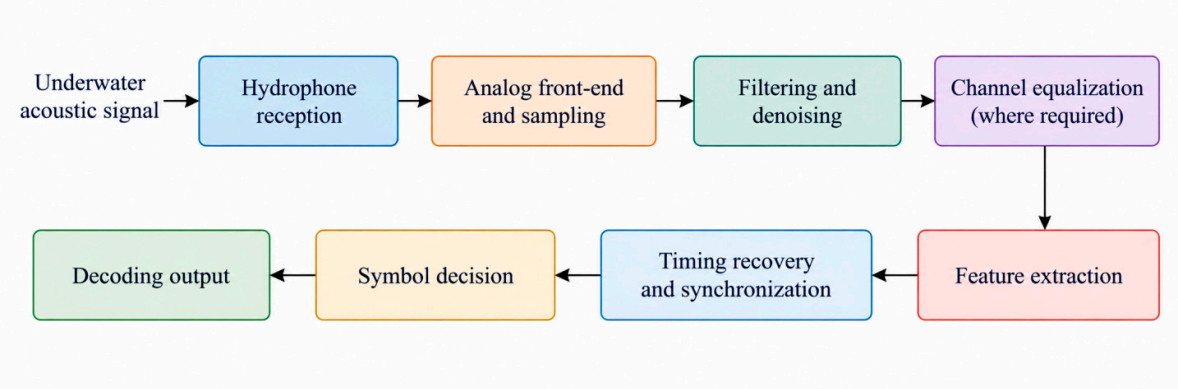


Figure 9. Receiver-processing chain for laser-induced acoustic communication.

4.2.1. Detection and Synchronization

Laser-induced acoustic signals often exhibit a prominent first peak, oscillatory tails, multiple peaks, and limited pulse-to-pulse consistency. Therefore, noise, multipath, and interface disturbances can cause missed detections and false alarms when a single amplitude threshold is used. Reliable synchronization requires stable waveform features from which pulse locations and symbol boundaries can be determined [99,100].

Peak detection is one representative approach. In PDOOK, Islam et al. used the first significant pressure peak for symbol detection and timing rather than tracking the entire oscillatory waveform, thereby reducing the influence of tails and multiple peaks on synchronization [84].

The receiver front end and preprocessing also affect timing performance. Zhao et al. used an optical-fiber underwater acoustic sensor to detect laser-generated sound,

illustrating the role of sensitive sensing in weak-signal acquisition and waveform preservation [99].

Wang et al. [100] developed a sliding-window nonlinear feature detector for laser-induced acoustic pulses. After estimating and subtracting a baseline from a signal-free interval and taking the absolute signal amplitude, the method tests three time-domain features describing a rapid rise and subsequent decay. Nearby candidate detections are consolidated, and a local amplitude maximum is used to refine pulse timing. The baseline estimate assumes nearly unchanged acquisition conditions; removing a constant offset should not be equated with suppressing all time-varying background noise.

The experiments compared pulse recognition in calm laboratory water and coastal water with waves over source–receiver distances of 5–25 m. At 5 m, the reported recognition rates were 98.5% and 92.3%, respectively; at 25 m, they fell to 75.6% and 42.4%. The authors identify limited noise tolerance and poorer recognition in complex underwater environments. These percentages describe pulse recognition, not decoded-bit BER or SER, and the paper does not quantify end-to-end data throughput or false-alarm probability [100]. Therefore, detection and synchronization should be treated jointly through sensing, preprocessing, feature extraction, and timing decisions, rather than threshold comparison alone.

Figure 10 provides a schematic illustration of the processing sequence. Filtering and preprocessing aim to reduce noise and unwanted trailing responses while preserving features used for detection, such as the first significant peak. Thresholds, peak positions, and symbol-boundary constraints are then combined to determine pulse timing and synchronize the receiver. The sequence of preprocessing, feature extraction, and timing recovery can be adapted to the modulation scheme, SNR, and severity of multipath [84,99,100]. The plotted waveforms illustrate these functions and do not quantify the performance of a particular algorithm.

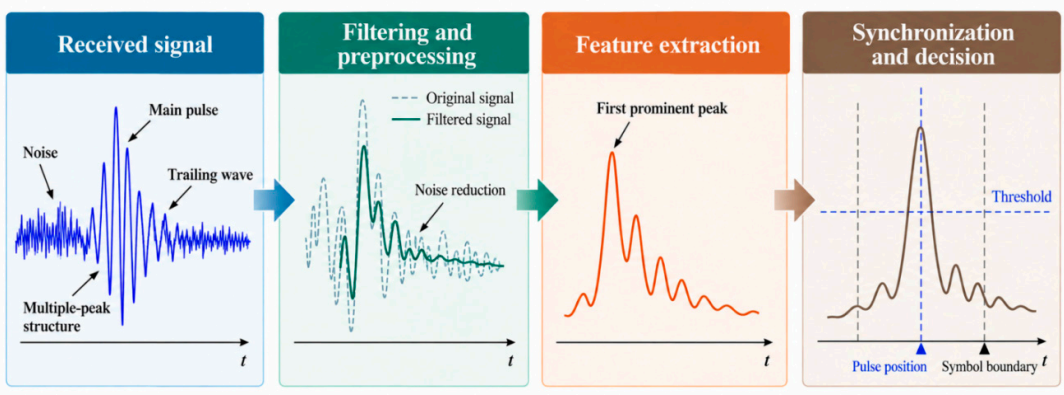


Figure 10. Schematic illustration of feature extraction, timing recovery, and symbol decisions for received laser-induced acoustic signals. The waveforms are illustrative and do not represent measured data.

4.2.2. Demodulation and Equalization

Demodulation and equalization address symbol distortion arising jointly from optoacoustic conversion and propagation. In addition to multipath, ambient noise, and intersymbol interference, the link is affected by conversion-induced pulse broadening, spectral redistribution, and variability in symbol waveforms under nonlinear excitation. Therefore, decisions based on a single amplitude sample may be insufficient; compensation must account for the modulation, waveform features, and channel response [11,99,101,102].

Noncoherent demodulation remains common for basic schemes such as OOK and PPM, using amplitude, envelope, or slot position as the decision feature. Despite its simplicity, its performance depends on the sensor frequency response, front-end bandwidth, filtering, and synchronization accuracy.

As multipath tails and waveform distortion increase, equalization can improve the signal presented to the detector. Fei et al. [101] investigated Sato blind equalization numerically for frequency-modulated optoacoustic signals. Their example used a 10,000-element random binary sequence, a 50-tap equalizer, a stated channel SNR of 20 dB, and an adaptation step of 0.002. The study reports reduced intersymbol interference and presents equalized sequences and a mean-square-error (MSE) trajectory. It does not report a measured communication distance or experimental BER improvement, and the plotted MSE evolution should not be interpreted as a strictly monotonic convergence law. The result supports receiver-side distortion compensation under the simulated conditions, not a demonstrated increase in source conversion efficiency or field-link robustness.

Mahmud et al. proposed a deep-learning-based method that jointly performs channel equalization and symbol detection, bringing distortion compensation and symbol identification into a single model [102]. These studies motivate joint treatment of channel distortion and symbol decisions, but their results should not be taken as comprehensive validation across sea states and platforms. Receiver design must account for both optoacoustic-source variability and underwater-channel distortion rather than assuming that conventional equalization transfers without adaptation [101,102].

4.2.3. Background Noise and SNR Management

Background noise limits both acquisition and symbol decisions, even when optoacoustic generation is repeatable. Natural sources include wind-driven surface processes, rain, and biological activity; human activities add shipping and other operational noise. The received background must also be distinguished from platform self-noise and hydrophone/electronic noise [103]. Regional measurements have documented increases in low-frequency ocean noise associated with shipping [104], but these observations should not be extrapolated to all locations, periods, or receiver bands. In warm shallow water, snapping-shrimp noise can be strongly non-Gaussian, and measured channels exhibit substantial time-varying multipath [105]. Consequently, an additive-white-Gaussian-noise simulation alone does not establish robustness to a real coastal soundscape.

The calm-water and wavy-water comparison in [100] provides laser-induced-acoustic evidence that pulse-recognition performance depends on the operating environment (Section 4.2.1). However, the comparison does not isolate background noise from surface-induced source changes or propagation effects. It supports environment-specific receiver testing, rather than a universal noise penalty or a claim of demonstrated BER robustness.

The PWM experiment of Chen et al. [87] provides a complementary, system-specific noise example. Its laboratory background was dominated by the laser water-cooling system; the receiver applied a high-pass filter and three band-pass filters before localization and decoding. Symbol decisions used segment-energy information, and the authors found that a threshold slightly below the segment mean reduced errors associated with pulse-energy fluctuations. This is evidence for the reported preprocessing and decision strategy, not a quantified universal SNR gain. The authors explicitly identify additional marine noise as a factor to consider outside the laboratory.

SNR should be defined at a specified receiver stage and over a stated bandwidth. For a transient link, the useful signal is the propagated, receiver-filtered waveform, not the original source pressure. Front-end and digital passbands should preserve the symbol-

bearing spectrum while excluding out-of-band noise; narrowing the band excessively can smear timing features or remove the frequency states needed for demodulation [38,99]. Correlation or matched-filter detection is a suitable candidate when a reliable pulse template is available; a white-noise matched filter is not automatically optimal for colored or impulsive noise. Template mismatch caused by bubbles, multipath, or source variability must be evaluated rather than assuming a fixed processing gain.

Practical receiver candidates include noise estimation during signal-free intervals, noise-adaptive decision thresholds, and rejection of persistent narrowband interference when the rejected band does not carry information. These measures should be assessed jointly with synchronization through missed-detection and false-alarm rates. Where receiver size and power permit, spatial filtering or diversity can also be considered, but benefits require validation under the actual noise directionality and channel conditions [38,105]. Such measures are design options drawn from acoustic receiver practice, not universally demonstrated improvements for the laser-induced links reviewed here.

Noise suppression, channel equalization, and coding should not be described as interchangeable SNR improvements. Equalization compensates for channel distortion and intersymbol interference but can amplify noise; error-control coding can lower BER at a given input SNR while adding redundancy and decoding cost. Repetition or averaging likewise trades energy and time for detection reliability and may be limited by channel changes and source recovery [38,96,97,101,102]. Therefore, reported gains should specify whether SNR is measured before or after filtering, whether noise is measured or artificially added, and how the noise spectrum and statistics were obtained. Error rates, synchronization failures, receiver bandwidth, and net information rate should be reported at the same operating point, with natural and anthropogenic background conditions identified.

4.3. Representative Experimental Systems and Scope of Validation

A typical experimental system comprises laser transmission, optoacoustic conversion, and underwater reception. Information is encoded in the laser pulses using OOK, PPM, or FSK; beam-delivery and focusing optics create an acoustic source in the water; and a hydrophone receives the signal for conditioning, acquisition, and demodulation, as shown in Figure 11. System assessment should distinguish source measurements, end-to-end information transfer, and proposed hardware configurations according to the stages actually validated.

Source-generation and reception measurements primarily validate the physical stages of the link. The laser/acoustic facility developed by Hickman and Edmonds provided a platform for optoacoustic conversion and acoustic-signal measurements [106]. In [107], a nanosecond Nd:YAG laser generated sound through optical breakdown, and a DFB-FL acoustic sensor received signals at different repetition rates. A numerical model was also used to analyze the acoustic field over longer underwater distances. The measured reception and long-range field simulation in that work must be interpreted separately: the latter does not establish experimentally demonstrated communication over the same range.

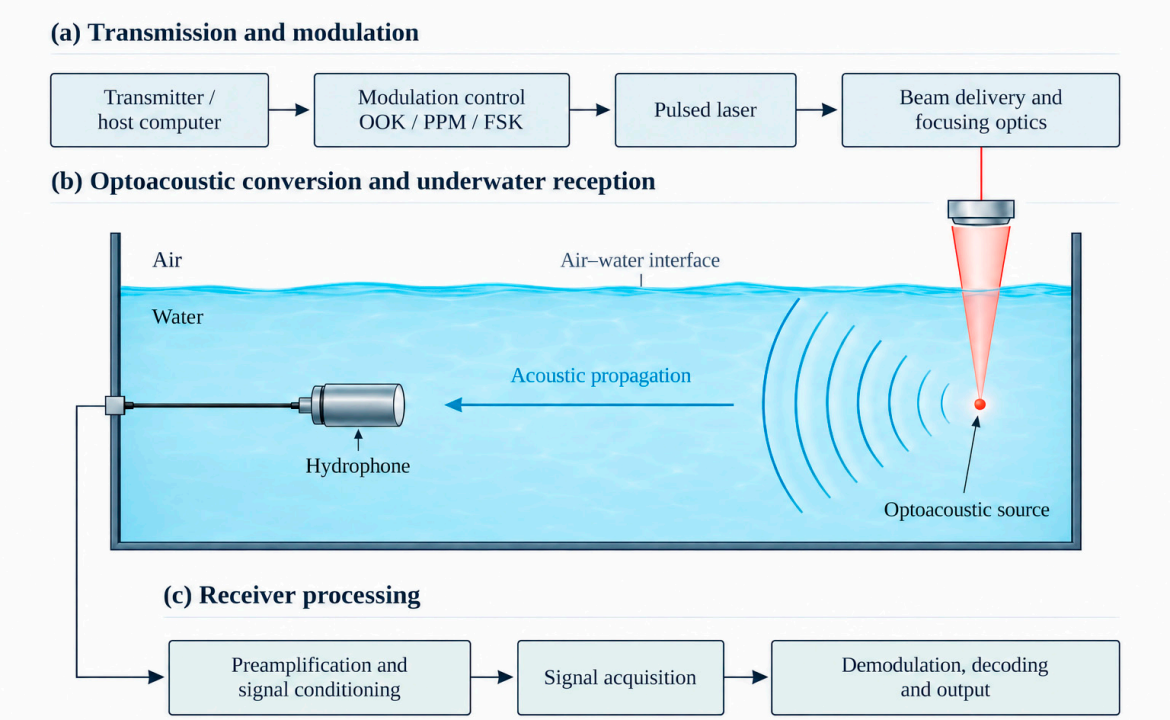


Figure 11. Representative experimental system for laser-induced acoustic air-to-underwater communication.

End-to-end communication experiments include information encoding, acoustic reception, and information recovery. Blackmon et al. demonstrated a linear optoacoustic downlink using laser excitation from the air and acoustic reception underwater [14], and Zhao et al. demonstrated direct air-to-underwater optoacoustic communication [12]. These results establish feasibility under the respective experimental conditions. Their range, error performance, and environmental applicability must nevertheless be interpreted within those conditions; a successful link trial does not establish reliability under complex sea conditions.

Zhao et al. [99] provide a further complete-link example rather than solely a receiver-sensitivity study. Their system uses thermal-expansion-based laser-generated sound, an underwater optical-fiber acoustic sensor, and OOK/PPM encoding. Phase demodulation, filtering, envelope extraction, and digital shaping support recovery of the transmitted information. This experiment links optical modulation, conversion, sensing, and decoding in one system. Therefore, its relevance is different from the broad surveys in [8,11] and from the shallow-water channel-prediction work in [68]; none of these evidence categories should substitute for validation of the others.

Source and system-configuration improvements mainly target acoustic output and compatibility among link components. Fan et al. [108] developed a mathematical model of modulated laser-acoustic symbols and derived modulation parameters for thermal-expansion and optical-breakdown excitation. Their design concentrates spectral energy at the modulation-characteristic frequencies and reduces the symbol bandwidth, rather than merely increasing acoustic peak pressure. This provides a source-design rationale for spectral tailoring; it should not be interpreted as a measured improvement in communication range or BER. Separately, an improved transduction system adjusts the transmitter structure, interface interaction, and receiver configuration to improve conversion and reception stability [109]. A cited patent proposes engineering arrangements for air-to-underwater communication, coordination of linear and nonlinear

mechanisms, and higher conversion efficiency [110]. Source enhancement, structural improvement, and proposed devices provide different forms of evidence and should not all be described as validated deployments.

Therefore, comparisons should specify what was validated, the test conditions, and the scope of the conclusions. Demonstrating a measurable source, recovering transmitted information, and validating a deployable system represent different levels of evidence. The controlled experiments and prototypes reviewed here provide a basis for subsequent system-level assessment; their engineering limitations are discussed in Section 5.2.

5. Applications and Limitations

Laser-induced acoustics offers non-contact information access from aerial platforms to underwater targets. The evidence reviewed here motivates further assessment of short-command transmission, node triggering, and communication through additional interfaces. High-rate, long-range continuous communication remains insufficiently validated. Figure 12 summarizes the application directions and engineering constraints.

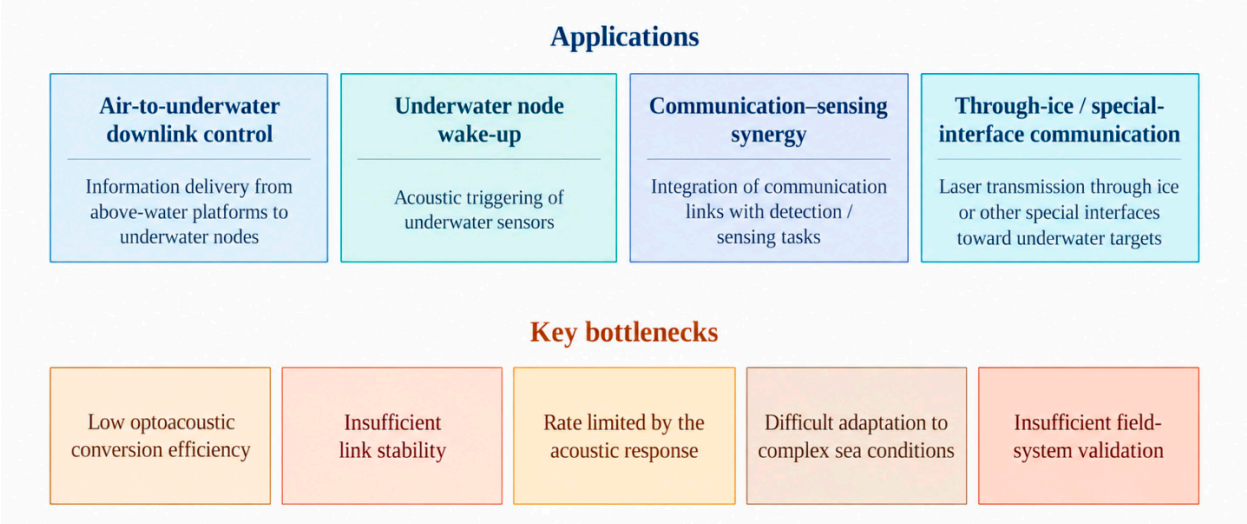


Figure 12. Application directions and key limitations of laser-induced acoustic air-to-underwater communication.

5.1. Application Scenarios

Downlink control is a direct application of the communication link. An airborne, shore-based, or other above-water platform transmits laser pulses that generate sound at the air–water interface or in near-surface water, and an underwater node receives the acoustic signal and recovers the transmitted information. Blackmon et al. demonstrated the feasibility of an aerial trans-layer downlink [111]. The low-cost passive-relay scheme proposed by Ji et al. [112], in contrast, is a relay-assisted approach and should be distinguished from direct acoustic generation in water. Potential messages include control codes, status commands, and emergency information for underwater-node access, task initiation, and operating-mode changes.

Remote wake-up of underwater nodes is a potential application of the downlink. Its requirements are compatible with short, low-rate, identifiable acoustic pulse sequences and motivate work on preamble acquisition, identity verification, and operating-mode switching. The communication-feasibility results reviewed here do not substitute for validation of a complete wake-up system. Triggering reliability, false-wake-up rate,

coverage, and the standby energy consumption of the entire receiver chain must be evaluated; a low data rate alone does not imply low power consumption.

Beyond communication, laser-induced acoustics has been investigated for remote excitation of underwater acoustic fields, including shallow-water bathymetry and imaging of small submerged targets [113,114]. Related airborne-sonar work has also addressed imaging under complex hydrodynamic conditions [48,54]. Non-contact thermoacoustic detection driven by radio-frequency excitation [115] uses a different excitation mechanism and should not be treated as direct validation of laser-induced acoustic applications. These studies provide technical context for non-contact acoustic access and sensing, but joint communication and sensing still require dedicated validation of waveform design, hardware sharing, and system scheduling.

Studies of additional interfaces have extended open-water configurations to transmission through ice-covered media. He et al. and Zhao et al. investigated air–ice–water configurations, providing a basis for information transfer under ice-covered conditions [116,117]. Hu et al. used finite-element analysis to study acoustic generation in this link and modeled the effects of ice parameters and interface conditions on propagation [118]. Experimental and numerical evidence should be identified separately; these results do not in themselves validate long-term polar operation or complete wake-up systems for under-ice equipment.

5.2. Technical Limitations

The main engineering challenge is the interaction among source strength, range, achievable data rate, and system complexity, rather than a limitation in any single acoustic metric [109]. Based on the preceding mechanisms and experimental evidence, the following discussion groups the limitations into energy utilization, timing and environmental disturbances, and system-level validation.

Range is constrained by end-to-end energy utilization. The energy budget includes losses during atmospheric transmission, interface coupling, optoacoustic conversion, and underwater propagation; losses at any stage reduce the received SNR. Evidence for stable, long-range operation in complex environments remains limited [109]. Coordinated sources are one possible response to an insufficient single-source pressure margin. Multiple-beam experiments show that beam number and spatial arrangement affect underwater shock-wave output [30]. However, these acoustic measurements do not establish improvements in communication range, error performance, or wake-up probability. Such gains require controlled comparisons between single- and multiple-source communication systems.

Achievable data rate is jointly limited by the acoustic-response duration, guard intervals, and receiver detection capability. Under nonlinear excitation, vapor-cloud and bubble evolution also affect subsequent optoacoustic conversion. Atmospheric turbulence, sea-surface motion, focal displacement, and underwater multipath cause amplitude and waveform shape to vary with environmental conditions, potentially leading to missed detections, false triggers, and timing offsets. Therefore, raising the modulation order or laser repetition rate alone cannot resolve timing and stability constraints. Suspended-particle and bubble populations can add frequency-dependent acoustic scattering, while natural and anthropogenic background noise changes the detection margin within the receiver band. These propagation and reception limitations remain relevant even after source conversion has been stabilized.

Limited system-level validation leaves a gap between laboratory performance and operational suitability. Most studies reviewed here use tanks, controlled surfaces, or short links. Link maintenance and parameter drift still need to be evaluated during platform motion, surface disturbances, and sustained operation, with underwater-node protocols

and power management included when defining the application scope. Acoustic measurements, information-transfer results, and task-execution outcomes should be reported separately so that a single successful transmission is not mistaken for long-term reliability.

6. Conclusions and Outlook

This review has examined laser-induced acoustic air-to-underwater communication through its generation mechanisms, propagation stages, laser-parameter effects, communication methods, and application constraints. The available evidence indicates that thermal expansion, vaporization, and optical breakdown should be compared in terms of source strength, repeatability, and modulation controllability. Communication capability depends on whether the acoustic response remains distinguishable after propagation, particle/bubble scattering, and background noise, within the effective bandwidth and time resolution of the receiver. Therefore, an increase in pressure, repetition rate, or symbol-set size alone is insufficient evidence of improved end-to-end performance.

A priority is to establish testable quantitative relationships among laser parameters, interface conditions, and received acoustic signals, with performance reported for clearly specified excitation conditions, propagation distances, and receiver configurations. Source measurements, propagation simulations, communication experiments, and proposed devices should be distinguished. Rates and error values obtained under different conditions should not be combined into a single performance result. Future validation should additionally document relevant particle/bubble conditions and the in-band noise spectrum, and separate source fluctuations from channel variability. Laboratory information recovery and simulated channel compensation do not, by themselves, establish robustness under realistic sea conditions.

Low-rate commands and node wake-up offer practical starting points for application-level validation. Their value must nevertheless be demonstrated through link availability, triggering reliability, and the standby energy consumption of the complete receiver chain. Therefore, engineering development should shift from isolated improvements in individual metrics toward repeatable, quantitative validation within clearly defined application boundaries.

Author Contributions: Y.Z.: conceptualization, supervision, funding acquisition, and writing—review and editing. Y.C.: investigation, writing—original draft preparation, and visualization. G.Z.: data curation and writing—original draft preparation. F.Z.: resources and investigation. Z.Z.: supervision, project administration, and funding acquisition. All authors have read and agreed to the published version of the manuscript.

Funding: This work was supported by the Shandong Provincial Natural Science Foundation (General Program), grant ZR2024MF082; the Major Cultivation Program of Harbin Institute of Technology, grant 2022FRFK01011; and the National Natural Science Foundation of China (No. U23A20379).

Institutional Review Board Statement: Not applicable. No studies involving human participants or animals were conducted for this review.

Informed Consent Statement: Not applicable.

Data Availability Statement: This review is based on published literature. The information summarized in the article and tables is supported by the cited references. No new experimental or simulation datasets were generated.

Acknowledgments: During the preparation and revision of this review, the authors used ChatGPT (GPT-5.6, OpenAI) to assist with grammar and spelling correction and the organization and refinement of selected sections. The authors reviewed and edited the AI-assisted content and take full responsibility for the content of the manuscript.

Conflicts of Interest: The authors declare no conflicts of interest.

References

1. Howe, B.M.; Chao, Y.; Arabshahi, P.; Roy, S.; McGinnis, T.; Gray, A. A smart sensor web for ocean observation: Fixed and mobile platforms, integrated acoustics, satellites and predictive modeling. *IEEE J. Sel. Top. Appl. Earth Obs. Remote Sens.* **2010**, *3*, 507–521. https://doi.org/10.1109/JSTARS.2010.2052022.
2. Premalatha, J.; Joe Prathap, P.M. A survey on underwater wireless sensor networks: Progresses, applications, and challenges. *Proc. MATEC Web Conf.* **2016**, *57*, 02007.
3. Yang, J.M.; Wang, J.H.; Qiao, G.; Liu, S.; Ma, L.; He, P. Review of Underwater Acoustic Communication and Network Technology. *J. Electron. Inf. Technol.* **2024**, *46*, 1–21. https://doi.org/10.11999/JEIT230424. (In Chinese)
4. Ali, M.F.; Jayakody, D.N.K.; Li, Y. Recent Trends in Underwater Visible Light Communication (UVLC) Systems. *IEEE Access* **2022**, *10*, 22169–22225. https://doi.org/10.1109/ACCESS.2022.3150093.
5. Islam, M.S.; Younis, M.F. Analyzing visible light communication through air-water interface. *IEEE Access* **2019**, *7*, 123830–123845.
6. Egerev, S.V. In search of a noncontact underwater acoustic source. *Acoust. Phys.* **2003**, *49*, 51–61. https://doi.org/10.1134/1.1537388.
7. Casari, P.; Zorzi, M. Protocol design issues in underwater acoustic networks. *Comput. Commun.* **2011**, *34*, 2013–2025. https://doi.org/10.1016/j.comcom.2011.06.008.
8. Hu, W.Y.; Jiang, H.Y.; Liao, X.; Wang, Y.; Li, X.; He, N. Review on laser-induced acoustic communication. *Infrared Laser Eng.* **2025**, *54*, 20250204. https://doi.org/10.3788/IRLA20250204. (In Chinese)
9. Lyamshev, L.M. Optoacoustic sources of sound. *Sov. Phys. Uspekhi* **1981**, *24*, 977–995. https://doi.org/10.1070/PU1981v024n12ABEH004757.
10. Sigrist, M.W. Laser generation of acoustic waves in liquids and gases. *J. Appl. Phys.* **1986**, *60*, R83–R122. https://doi.org/10.1063/1.337089.
11. Mahmud, M.; Islam, M.S.; Ahmed, A.; Younis, M.; Choa, F.S. Cross-Medium Photoacoustic Communications: Challenges, and State of the Art. *Sensors* **2022**, *22*, 4224. https://doi.org/10.3390/s22114224.
12. Zhao, Y.; Huang, J.; Zhang, P.; Cao, Y.; Zhou, Z. Direct air-water communication by using an optical-acoustic method. *Measurement* **2023**, *223*, 113824. https://doi.org/10.1016/j.measurement.2023.113824.
13. He, D.M. High-power Nd:YAG-generated underwater sound source for air-submarine communication. In *Proceedings of Solid State Lasers VIII*; SPIE: Bellingham, WA, USA, 1999; Volume 3613, pp. 83–92. https://doi.org/10.1117/12.347685.
14. Blackmon, F.; Estes, L.; Fain, G. Linear optoacoustic underwater communication. *Appl. Opt.* **2005**, *44*, 3833–3845. https://doi.org/10.1364/AO.44.003833.
15. He, Q.Y.; Zong, S.G. Analysis and perspectives on the development of laser-acoustic technology across the air–water interface. *Laser Infrared* **2019**, *49*, 3–8. (In Chinese)
16. Huang, L.L.; He, N.; Feng, T.Q.; He, Z.Y. Research on underwater acoustic communication of laser acoustic downlink through air-sea transmission channel. *Laser Infrared* **2014**, *44*, 972–976. Available online: http://magazine.laser-infrared.com/jgyhw/article/abstract/m440903 (accessed on 12 November 2026). (In Chinese)
17. Zhao, Z.H.; Xin, H.Y.; Wang, X.Y. A preliminary study of communication using laser-induced acoustic signals. *Infrared Laser Eng.* **2015**, *44*, 863–866. (In Chinese)
18. Blackmon, F.; Antonelli, L.; Carapezza, E. Remote, aerial, opto-acoustic communications and sonar. In *Proceedings of Sensors, and Command, Control, Communications, and Intelligence (C3I) Technologies for Homeland Security and Homeland Defense IV*; SPIE: Bellingham, WA, USA, 2005; Volume 5778, pp. 800–808.
19. Cui, G.H.; Li, R.F.; Li, G.J. Research on laser-induced acoustic technology and its application prospects. *Acoust. Electron. Eng.* **1989**, No. 2, 17–22. (In Chinese)
20. Su, K.; Ren, D.H.; Li, J.; You, Z.; Wang, Z. Study on laser generating ultrasonic waves. *Opto-Electron. Eng.* **2002**, *29*, 68–72. (In Chinese)

21. Chen, Q.M.; Cheng, Z.H. Research of laser acoustic effect in liquid. *Laser Infrared* **2006**, *36*, 623–626. (In Chinese)
22. Sigrist, M.W.; Kneubühl, F.K. Laser-generated stress waves in liquids. *J. Acoust. Soc. Am.* **1978**, *64*, 1652–1663. https://doi.org/10.1121/1.382132.
23. Aussel, J.D.; Le Brun, A.; Baboux, J.C. Generating acoustic waves by laser: Theoretical and experimental study of the emission source. *Ultrasonics* **1988**, *26*, 245–255.
24. Hoelen, C.G.A.; De Mul, F.F.M. A new theoretical approach to photoacoustic signal generation. *J. Acoust. Soc. Am.* **1999**, *106*, 695–706. https://doi.org/10.1121/1.427087.
25. Ye, H.; Chen, G.X.; Liu, Y.; Wang, J.L.; Pan, X.; Cheng, X.W.; Li, F.Q.; Xu, W.; Chen, W.B.; Zhang, W. Mechanism of time-domain waveform generation for planar acoustic sources induced by laser thermal expansion. *Acta Opt. Sin.* **2025**, *45*, 1014002. https://doi.org/10.3788/AOS250572. (In Chinese)
26. Zhang, S.; Cheng, X.J.; He, Y.; Shang, J.H. Study on the acoustic wave characteristics of laser-induced underwater sound under thermal expansion mechanism. *J. Optoelectron. Laser* **2026**, *Advance Online Publication*. Available online: https://link.cnki.net/urlid/12.1182.O4.20260417.1045.028 (accessed on 12 November 2026). (In Chinese)
27. Blackmon, F.; Antonelli, L. Experimental demonstration of multiple pulse nonlinear optoacoustic signal generation and control. *Appl. Opt.* **2005**, *44*, 103–112. https://doi.org/10.1364/AO.44.000103.
28. Li, K.; Liang, J.P.; Yao, Y.; Yang, Z.; Zong, S.; Tao, L. Three-dimensional numerical characteristics of optical-to-acoustic transboundary communication in vaporization mechanism. *Infrared Laser Eng.* **2023**, *52*, 20230100. (In Chinese) https://doi.org/10.3788/IRLA20230100
29. Tagawa, Y.; Yamamoto, S.; Hayasaka, K.; Kameda, M. On pressure impulse of a laser-induced underwater shock wave. *J. Fluid Mech.* **2016**, *808*, 5–18.
30. Yang, Z.; Bao, H.; Dai, L.; Zhang, H.; Lu, J. Experimental investigation of nanosecond laser-induced shock waves in water using multiple excitation beams. *Opt. Express* **2023**, *31*, 21845–21862. https://doi.org/10.1364/OE.492613.
31. Noack, J.; Vogel, A. Laser-induced plasma formation in water at nanosecond to femtosecond time scales: Calculation of thresholds, absorption coefficients, and energy density. *IEEE J. Quantum Electron.* **1999**, *35*, 1156–1167. https://doi.org/10.1109/3.777215.
32. Vogel, A.; Nahen, K.; Theisen, D.; Noack, J. Plasma formation in water by picosecond and nanosecond Nd:YAG laser pulses. I. Optical breakdown at threshold and superthreshold irradiance. *IEEE J. Sel. Top. Quantum Electron.* **1996**, *2*, 847–860. https://doi.org/10.1109/2944.577307.
33. Vogel, A.; Busch, S.; Parlitz, U. Shock wave emission and cavitation bubble generation by picosecond and nanosecond optical breakdown in water. *J. Acoust. Soc. Am.* **1996**, *100*, 148–165. https://doi.org/10.1121/1.415878.
34. Sinibaldi, G.; Occhicone, A.; Alves Pereira, F.; Caprini, D.; Marino, L.; Michelotti, F.; Casciola, C.M. Laser induced cavitation: Plasma generation and breakdown shockwave. *Phys. Fluids* **2019**, *31*, 103302. https://doi.org/10.1063/1.5119794.
35. Wu, W.; Chai, S.; Zhou, Y. Acoustic characteristics of laser-induced plasmas from the forming dynamics perspective. *Appl. Opt.* **2023**, *62*, 9375–9382. https://doi.org/10.1364/AO.506394.
36. Zong, S.G.; Wang, J.A.; Wang, Y.H. Experiment investigation of water breakdown characteristic by high power laser. *Opto-Electron. Eng.* **2008**, *35*, 68–72. (In Chinese)
37. Lu, G.; Liu, T.; Chen, B. Research on laser-acoustic energy conversion efficiency in different focusing conditions. *Equip. Manuf. Technol.* **2015**, No. 9, 1–3, 15. (In Chinese)
38. Stojanovic, M. Underwater acoustic communications: Design considerations on the physical layer. In *Proceedings of 2008 Fifth Annual Conference on Wireless on Demand Network Systems and Services*; IEEE: Piscataway, NJ, USA, 2008; pp. 1–10. https://doi.org/10.1109/WONS.2008.4459349.
39. Al-Aish, T.A.K.; Saleh, M.K. Simulation and analysis the attenuation effect of atmospheric layers on a laser beam within the visible range. *Ibn Al-Haitham J. Pure Appl. Sci.* **2023**, *36*, 124–136. https://doi.org/10.30526/36.3.3093.
40. Fahey, T.; Islam, M.; Gardi, A.; Sabatini, R. Laser beam atmospheric propagation modelling for aerospace LIDAR applications. *Atmosphere* **2021**, *12*, 918. https://doi.org/10.3390/atmos12070918.
41. Al Naboulsi, M.C.; Sizun, H.; De Fornel, F. Fog attenuation prediction for optical and infrared waves. *Opt. Eng.* **2004**, *43*, 319–329. https://doi.org/10.1117/1.1637611.
42. Ishimaru, A. *Wave Propagation and Scattering in Random Media*; Academic Press: New York, NY, USA, 1978.
43. Gan, X.J.; Guo, J.; Wang, B.; Fu, Y.Y. Attenuation prediction for 1.06 μm laser propagation in the troposphere. *J. Changchun Univ. Sci. Technol.* **2006**, *29*, 8–10, 13. (In Chinese)

44. Wang, H.; Zhang, T. Analysis of performance for free-space optical communications with rain or fog weather condition. *Laser Optoelectron. Prog.* **2012**, *49*, 080101. https://doi.org/10.3788/LOP49.080101. (In Chinese)
45. Jafari, M.; Mollaee, M.; Magham, K.H.J.; Rokanabadi, M.R. Analysis of laser beam propagation through atmospheric turbulence and its impact on CCD sensor intensity distribution. *J. Atmos. Sol.-Terr. Phys.* **2025**, *271*, 106527. https://doi.org/10.1016/j.jastp.2025.106527.
46. Zhao, J.; Yu, K.; Xu, S.; Wang, M.; Yang, Y.; Xu, D.; Yao, J.; Wang, X. Advances in laser-induced acoustic technology for underwater detection. *Water* **2025**, *17*, 3285. https://doi.org/10.3390/w17223285.
47. Li, P.; Zhao, Y.; Zhou, Z.Q.; Zhang, P.; Bai, X.; Ma, J. Research on laser induced acoustic detection of trans-media aerial-underwater. *Infrared Laser Eng.* **2021**, *50*, 20200310. https://doi.org/10.3788/IRLA20200310. (In Chinese)
48. Fitzpatrick, A.; Singhvi, A.; Arbabian, A. An airborne sonar system for underwater remote sensing and imaging. *IEEE Access* **2020**, *8*, 189945–189959. https://doi.org/10.1109/ACCESS.2020.3031808.
49. Hornstein, M.K.; Jones, T.G.; Ting, A.C.; Lindwall, D. Optical bandwidth and focusing dynamics effects on an underwater laser acoustic source. In *Proceedings of Conference on Lasers and Electro-Optics/International Quantum Electronics Conference*; IEEE: Piscataway, NJ, USA, 2009; Paper CMQ1. https://doi.org/10.1364/CLEO.2009.CMQ1.
50. Zong, S.; Wang, J.; Jiang, X.; Wang, Y.H. Characteristics of laser-induced acoustic wave at different laser focusing position. *Laser Technol.* **2009**, *33*, 269–272. (In Chinese)
51. Zong, S.G.; Wang, J.A.; Wang, Y.H. Laser-induced acoustic-source characteristics and marine applications. *J. Appl. Opt.* **2008**, *29*, 408–411. (In Chinese)
52. Jones, T.G.; Helle, M.; Ting, A.; Nicholas, M. Tailoring underwater laser acoustic pulses. *NRL Rev.* **2012**, 142–143.
53. Yu, Y.; Wang, J.A.; Jiang, X.Z. The study of theory of directivity of laser-induced sound radiating field in water. *Laser Infrared* **2007**, *37*, 26–28, 31. (In Chinese)
54. Fitzpatrick, A.; Mathews, R.P.; Singhvi, A.; Arbabian, A. Multi-modal sensor fusion towards three-dimensional airborne sonar imaging in hydrodynamic conditions. *Commun. Eng.* **2023**, *2*, 16. https://doi.org/10.1038/s44172-023-00065-4.
55. Shi, X.; Gao, X.; Hussain, A.; Lin, J. The effect of distance between lens and water surface on the acoustic characteristics induced by a 532 nm nanosecond laser under water. *Results Opt.* **2021**, *2*, 100053.
56. Liu, Q.; Song, W.; Tian, Y.; Zhang, Z.; Yuan, G. On the reproducibility and directionality of underwater laser-induced acoustic signal. *J. Phys. Conf. Ser.* **2023**, *2486*, 012064.
57. Yang, C.F.; Liu, Z.; Wei, J.H.; Yu, S.; Fu, Q.; Wang, C. A scanning focal-point method for enhancing the signal stability of laser-induced acoustic communication. *Optics* **2026**, *7*, 44. https://doi.org/10.3390/opt7030044.
58. Khan, M.R.; Das, B.; Pati, B.B. Channel estimation strategies for underwater acoustic (UWA) communication: An overview. *J. Frankl. Inst.* **2020**, *357*, 7229–7265. https://doi.org/10.1016/j.jfranklin.2020.04.002.
59. Kiselev, V.D.; Maksimov, A.O. Dispersion deformation of optoacoustic pulses in the surface layer of the ocean. *J. Appl. Mech. Tech. Phys.* **1993**, *34*, 796–801.
60. Qarabaqi, P.; Stojanovic, M. Statistical characterization and computationally efficient modeling of a class of underwater acoustic communication channels. *IEEE J. Ocean. Eng.* **2013**, *38*, 701–717. https://doi.org/10.1109/JOE.2013.2278787.
61. Yellaiah, J.; Prem Kiran, P. Input pulse duration effect on laser-induced underwater acoustic signals. *Appl. Opt.* **2021**, *60*, 4582–4590. https://doi.org/10.1364/AO.422471.
62. Yellaiah, J. Characterization of nanosecond laser-induced underwater filamentation using acoustic measurements. *Appl. Opt.* **2022**, *61*, 9685–9692. https://doi.org/10.1364/AO.473264.
63. Li, S.Y.; Wu, R.H.; Wang, X.Y.; Wang, J.; Zong, S. Properties of laser-induced acoustic signals transmission in liquid. *Infrared Laser Eng.* **2017**, *46*, 0406006. https://doi.org/10.3788/IRLA201746.0406006. (In Chinese)
64. Moate, B.D.; Thorne, P.D. Scattering from suspended sediments having different and mixed mineralogical compositions: Comparison of laboratory measurements and theoretical predictions. *J. Acoust. Soc. Am.* **2013**, *133*, 1320–1334. https://doi.org/10.1121/1.4788985.
65. Commander, K.W.; Prosperetti, A. Linear pressure waves in bubbly liquids: Comparison between theory and experiments. *J. Acoust. Soc. Am.* **1989**, *85*, 732–746. https://doi.org/10.1121/1.397599.
66. Ostashev, V.E.; Wilson, D.K. *Acoustics in Moving Inhomogeneous Media*, 3rd ed.; CRC Press: Boca Raton, FL, USA, 2026.
67. Zhao, J.; Zhang, Y.; Lv, M.; Zhao, L.; Wang, M.; Yang, Y.; Wang, X. Experimental research on characteristics of laser induced underwater acoustic signals. In *Proceedings of Fourth International Computational Imaging Conference (CITA 2024)*; SPIE: Bellingham, WA, USA, 2025; Volume 13542, p. 135421X. https://doi.org/10.1117/12.3055651.

68. Busacca, F.; Galluccio, L.; Palazzo, S.; Panebianco, A. A comparative analysis of predictive channel models for real shallow water environments. *Comput. Netw.* **2024**, *250*, 110557. https://doi.org/10.1016/j.comnet.2024.110557.
69. Ramley, I.; Alzayed, H.M.; Al-Hadeethi, Y.; Chen, M.; Barasheed, A.Z. An overview of underwater optical wireless communication channel simulations with a focus on the Monte Carlo method. *Mathematics* **2024**, *12*, 3904. https://doi.org/10.3390/math12243904.
70. Yuan, R.; Zhang, T.; Li, C.; Gao, H.; Hu, L. Laser transmission characteristics of seawater for underwater wireless optical communication. *Sensors* **2025**, *25*, 3057. https://doi.org/10.3390/s25103057.
71. Li, H.; Zhu, J.; Deng, J.; Guo, F.; Sun, J.; Zhang, Y.; Hou, X. Influence mechanism of the particle size on underwater active polarization imaging of reflective targets. *Opt. Express* **2023**, *31*, 7212–7225. https://doi.org/10.1364/OE.483632.
72. Jang, H.; Song, H.; Koh, H.S.; Yoon, T.; Kwon, Y.J. Shock wave generation in water by nanosecond pulse laser irradiation with 1064 and 2940 nm wavelengths. *Opt. Laser Technol.* **2023**, *167*, 109670. https://doi.org/10.1016/j.optlastec.2023.109670.
73. Zhang, T.; Cao, X.; Tan, Q.; Yang, Y.; Du, Y.; Yuan, J.; Cui, T.; Yao, J. Study on the influence of water color on signal directionality in laser-induced acoustic processes. *J. Mar. Sci. Eng.* **2025**, *13*, 552.
74. Yellaiah, J. Characteristics of nanosecond laser-induced underwater acoustic signals across the water-air interface. *Acoust. Phys.* **2023**, *69*, 7–19. https://doi.org/10.1134/S1063771022600437.
75. Brelet, Y.; Jarnac, A.; Carbonnel, J.; André, Y.B.; Mysyrowicz, A.; Houard, A.; Fattaccioli, D.; Guillermin, R.; Sessarego, J.P. Underwater acoustic signals induced by intense ultrashort laser pulse. *J. Acoust. Soc. Am.* **2015**, *137*, EL288–EL292. https://doi.org/10.1121/1.4914998.
76. Houard, A.; Brelet, Y.; Jarnac, A.; Carbonnel, J.; Mysyrowicz, A.; Milian, C.; Couairon, A.; Guillermin, R.; Sessarego, J.P. Propagation of intense femtosecond laser pulse in water and acoustic waves generation. In *Proceedings of 2014 Conference on Lasers and Electro-Optics*; Optica Publishing Group: Washington, DC, USA, 2014; Paper STh1E.8. https://doi.org/10.1364/CLEO_SI.2014.STh1E.8.
77. Jukna, V.; Jarnac, A.; Milián, C.; Brelet, Y.; Carbonnel, J.; André, Y.B.; Guillermin, R.; Sessarego, J.P.; Fattaccioli, D.; Mysyrowicz, A.; et al. Underwater acoustic wave generation by filamentation of terawatt ultrashort laser pulses. *Phys. Rev. E* **2016**, *93*, 063106. https://doi.org/10.1103/PhysRevE.93.063106.
78. Jukna, V.; Albert, S.; Millon, C.; Mahieu, B.; Guillermin, R.; Rabau, G.; Fattaccioli, D.; Mysyrowicz, A.; Couairon, A.; Houard, A. Control of the acoustic waves generated by intense laser filamentation in water. *Opt. Express* **2022**, *30*, 9103–9111. https://doi.org/10.1364/OE.453749.
79. Ravishankar, S.R.; Jones, B.E. Laser generated acoustic emission in water. *NDT E Int.* **2007**, *40*, 602–608.
80. Berthelot, Y.H. Thermoacoustic generation of narrow-band signals with high repetition rate pulsed lasers. *J. Acoust. Soc. Am.* **1989**, *85*, 1173–1181. https://doi.org/10.1121/1.397447.
81. Kaleris, K.; Hatziantoniou, P.; Stelzner, B.; Trimis, D. Laser-sound reproduction by pulse amplitude modulation audio streams. *Sci. Rep.* **2024**, *14*, 12102. https://doi.org/10.1038/s41598-024-62382-8.
82. Peng, S.; Zhang, M.; Wang, J. Method of laser-generated sound with high repetition rate for underwater acoustic communication. *Chin. J. Lasers* **2012**, *39*, 0705005. (In Chinese)
83. Jiang, H.; Qiu, H.; He, N.; Liao, X. Research on the optoacoustic communication system for speech transmission by variable laser-pulse repetition rates. *Results Phys.* **2018**, *9*, 1291–1296. https://doi.org/10.1016/j.rinp.2018.04.050.
84. Islam, M.S.; Younis, M.; Mahmud, M.; Carter, G.; Choa, F.S. A peak detection based OOK photoacoustic modulation scheme for air to underwater communication. *Opt. Commun.* **2023**, *529*, 129078.
85. Islam, M.S.; Younis, M.; Mahmud, M.; Choa, F.S. An efficient pulse position modulation scheme to improve the bit rate of photoacoustic communication. In *Proceedings of 2023 32nd Wireless and Optical Communications Conference (WOCC)*; IEEE: Piscataway, NJ, USA, 2023; pp. 1–6.
86. Liao, X.; Jiang, H.Y.; He, N. Underwater time slot-hopping data transmission based on laser-induced acoustic waves. *Chin. J. Lasers* **2022**, *49*, 1806002. https://doi.org/10.3788/CJL202249.1806002. (In Chinese)
87. Chen, Y.N.; Zhao, Y.; Zhou, Z.Q.; Cao, Y.F.; Zhang, F.X. Laser-induced acoustic air-water trans-medium communication based on PWM. *J. Unmanned Undersea Syst.* **2024**, *32*, 637–643. https://doi.org/10.11993/j.issn.2096-3920.2024-0019. (In Chinese)
88. Mahmud, M.; Younis, M.; Islam, M.S.; Choa, F.S.; Carter, G. Vapor cloud delayed-DPPM modulation technique for nonlinear optoacoustic communication. In *Proceedings of GLOBECOM 2022–2022 IEEE Global Communications Conference*; IEEE: Piscataway, NJ, USA, 2022; pp. 819–824.
89. He, N.; Feng, T.Q.; Huang, L.L. Research on underwater laser acoustic communication based on tunable fundamental frequency. *Optoelectron. Technol.* **2015**, *35*, 18–22. (In Chinese) https://doi.org/10.19453/j.cnki.1005-488x.2015.01.005.

90. Zhou, Z.Q.; Zhao, X.K.; Chen, Y.N.; Huang, J.X.; Zhao, Y. Algorithm of water-air trans-medium communication based on acousto-optic system. *J. Unmanned Undersea Syst.* **2024**, *32*, 644–649, 658. https://doi.org/10.11993/j.issn.2096-3920.2024-0098. (In Chinese)
91. Huang, J.X.; Zhou, Z.Q.; Cao, Y.F.; Zhao, Y. Method of laser-generated sound with *n*-MFSK modulation for air-water trans-media communication. *Laser Technol.* **2024**, *48*, 8–13. https://doi.org/10.7510/jgjs.issn.1001-3806.2024.01.002. (In Chinese)
92. Chen, Y.N.; Zhao, Y.; Zhou, Z.Q.; Wang, X.; Zhang, Y.; Zhang, F. Improving reliability of laser-generated sound across-media communication by FSK method. *Meas. Sci. Technol.* **2025**, *36*, 085204. https://doi.org/10.1088/1361-6501/adf247.
93. Harbin Institute of Technology (Weihai). Air-to-Water Cross-Medium Laser-Induced Acoustic Communication Method and Device Based on PPM-FSK Modulation. Chinese Patent CN117579169B, 16 July 2024. (In Chinese)
94. Harbin Institute of Technology (Weihai). Cross-Medium Laser-Induced Acoustic Communication Method and Device Based on PWM-FSK Modulation. Chinese Patent CN117579168B, 9 July 2024. (In Chinese)
95. Mahmud, M.; Younis, M.; Choa, F.S.; Ahmed, A. Optical focusing-based adaptive modulation for air-to-underwater optoacoustic communication. *IEEE Sens. J.* **2024**, *24*, 8596–8614. https://doi.org/10.1109/JSEN.2023.3340092.
96. Harbin Institute of Technology (Weihai). Air-to-Water Cross-Medium Laser-Induced Acoustic Communication Method Based on Manchester Coding. Chinese Patent CN116318436B, 28 June 2024. (In Chinese)
97. Harbin Institute of Technology (Weihai). Air-to-Water Cross-Medium Laser Communication Method and Device Based on Quasi-Cyclic Low-Density Parity-Check (QC-LDPC) Coding. Chinese Patent CN115499069B, 20 August 2024. (In Chinese)
98. Hu, M.; Tan, Q.; Zhao, Z.; Zhong, S.; Xu, H.; Yang, Y.; Yao, J. Cross-medium transmission method based on 8B/10B special position coding. *IEEE Access* **2025**, *13*, 40943–40949. https://doi.org/10.1109/ACCESS.2025.3546289.
99. Zhao, Y.; Chen, Y.; Huang, J.; Zhou, Z.; Zhang, F. Photoacoustic communication system based on detecting laser-generated sound by optical fiber underwater acoustic sensor. *Opt. Lasers Eng.* **2024**, *177*, 108134. https://doi.org/10.1016/j.optlaseng.2024.108134.
100. Wang, Y.C.; Han, D.; Li, L. A nonlinear-filter-based method for identifying laser-induced acoustic signals. *Sci. Technol. Innov.* **2021**, 75–76. (In Chinese)
101. Fei, Z.G.; Peng, S.; Chen, B.Z. Study on equalization algorithm based on opto-acoustic underwater communication. *Mar. Electr. Electron. Eng.* **2018**, *38*, 18–20, 24. https://doi.org/10.13632/j.meee.2018.12.005. (In Chinese)
102. Mahmud, M.; Younis, M.; Ahmed, M.; Choa, F.S. Deep learning-based joint channel equalization and symbol detection for air-water optoacoustic communications. *IEEE Trans. Cogn. Commun. Netw.* **2025**, *11*, 1482–1492. https://doi.org/10.1109/TCCN.2024.3480036.
103. Wenz, G.M. Acoustic Ambient Noise in the Ocean: Spectra and Sources. *J. Acoust. Soc. Am.* **1962**, *34*, 1936–1956. https://doi.org/10.1121/1.1909155.
104. McDonald, M.A.; Hildebrand, J.A.; Wiggins, S.M. Increases in deep ocean ambient noise in the Northeast Pacific west of San Nicolas Island, California. *J. Acoust. Soc. Am.* **2006**, *120*, 711–718. https://doi.org/10.1121/1.2216565.
105. Chitre, M. A high-frequency warm shallow water acoustic communications channel model and measurements. *J. Acoust. Soc. Am.* **2007**, *122*, 2580–2586. https://doi.org/10.1121/1.2782884.
106. Hickman, G.D.; Edmonds, J.A. *An Experimental Facility for Laser/Acoustic Applications*; Interim Report AST-R-151181; Applied Science Technology, Inc.: Arlington, VA, USA, 1981; DTIC Accession No. AD-A110872.
107. Zhao, Y.; Li, P.; Zhang, P.H.; Zhou, Z.; Li, J. Application of laser-induced acoustic method on air-underwater communication. In *Proceedings of 2021 International Conference on Space-Air-Ground Computing (SAGC)*; IEEE: Piscataway, NJ, USA, 2021; pp. 77–82. https://doi.org/10.1109/SAGC52752.2021.00020.
108. Fan, D.Y.; Zhang, M.M.; Peng, S. A source design method for underwater laser-acoustic communication. *Laser Technol.* **2013**, *37*, 371–375. https://doi.org/10.7510/jgjs.issn.1001-3806.2013.03.023. (In Chinese)
109. Chen, Y.; Zhou, Z.; Zhang, Y.; Wang, X.; Zhao, Y. An improved optoacoustic system for signal cross-medium transduction. *J. Phys. Conf. Ser.* **2025**, *2966*, 012001. https://doi.org/10.1088/1742-6596/2966/1/012001.
110. Harbin Institute of Technology (Weihai). Cross-Medium Air-to-Underwater Laser-Induced Acoustic Communication Method and Device. Chinese Patent CN113556177B, 4 July 2023. (In Chinese)
111. Blackmon, F.; Antonelli, L. Remote, aerial, trans-layer, linear and non-linear downlink underwater acoustic communication. In *Proceedings of OCEANS 2006*; IEEE: Piscataway, NJ, USA, 2006; pp. 1–7.
112. Ji, Z.; Fu, Y.; Li, J.; Zhao, Z.; Mai, W. Photoacoustic communication from the air to underwater based on low-cost passive relays. *IEEE Commun. Mag.* **2021**, *59*, 140–143. https://doi.org/10.1109/MCOM.001.2000607.

113. Hickman, G.D.; Edmonds, J.A. Laser-acoustic measurements for remotely determining bathymetry in shallow turbid waters. *J. Acoust. Soc. Am.* **1983**, *73*, 840–843. https://doi.org/10.1121/1.389052.
114. Zhao, Y.; Li, P.; Zhang, P.H.; Zhou, Z.Q.; Bai, X.; Ma, J. Underwater Small Target Detection Method of Laser-Induced Acoustic SAFT Based on PSM Algorithm. *Chin. J. Lasers* **2022**, *49*, 0909001. (In Chinese)
115. Nan, H.; Boyle, K.C.; Apte, N.; Aliroteh, M.S.; Bhuyan, A.; Nikoozadeh, A.; Khuri-Yakub, B.T.; Arbabian, A. Non-contact thermoacoustic detection of embedded targets using airborne-capacitive micromachined ultrasonic transducers. *Appl. Phys. Lett.* **2015**, *106*, 084101. https://doi.org/10.1063/1.4909508.
116. He, N.; Liao, X.; Jiang, H.Y. Application of laser-induced acoustics to air-to-underwater communication through ice. *Laser Infrared* **2023**, *53*, 1644–1649. (In Chinese)
117. Zhao, Y.; Chen, Y.; Zhang, F.; Wang, X.; Zhou, Z.; Zhang, Y. Air-ice-water cross-media communication by using laser-generated sound technology. *Appl. Acoust.* **2025**, *231*, 110511.
118. Hu, W.Y.; Jiang, H.Y.; Li, Z.J.; Li, X.; Deng, D. Finite element analysis of laser-induced acoustic characteristics for air-to-water cross-ice communication. In *Proceedings of AOPC 2025: Laser Technology and Applications*; Zhou, P., Ed.; SPIE: Bellingham, WA, USA, 2025; Volume 13956, p. 139560R. https://doi.org/10.1117/12.3083612.

Disclaimer/Publisher's Note: The statements, opinions and data contained in all publications are solely those of the individual author(s) and contributor(s) and not of MDPI and/or the editor(s). MDPI and/or the editor(s) disclaim responsibility for any injury to people or property resulting from any ideas, methods, instructions or products referred to in the content.